2012

Computational Investigation of a Hinge-Connected Hovering Plate

Zachary Robert Gaston
Wright State University

COMPUTATIONAL INVESTIGATION OF A HINGE-CONNECTED HOVERING PLATE

A thesis submitted in partial fulfillment

of the requirements for the degree of

Master of Science in Engineering

By

ZACHARY ROBERT GASTON

B.S., Wright State University, 2011

2012

Wright State University

WRIGHT STATE UNIVERSITY

GRADUATE SCHOOL

Wednesday May 30, 2012

I HEREBY RECOMMEND THAT THE THESIS PREPARED UNDER MY SUPERVISION BY Zachary Robert Gaston ENTITLED Computational Investigation of a Hinge-Connected Hovering Plate BE ACCEPTED IN PARTIAL FULFILLMENT OF THE REQUIREMENTS FOR THE DEGREE OF Master of Science in Engineering.

Committee on
Final Examination

Hui Wan, Ph.D.

Haibo Dong, Ph.D.
Thesis Director

Zifeng Yang, Ph.D.

George Huang, Ph.D.
Chair
Department of Mechanical and Materials Engineering
College of Engineering and Computer Science

Andrew Hsu, Ph.D.
Dean, Graduate School

ABSTRACT

Gaston, Zachary Robert. M.S.Egr. Department of Mechanical and Materials Engineering, Wright State University, 2012. Computational Investigation of a Hinge-connected Hovering Plate.

A simplified conceptual flapping wing MAV design, capable of hover, is formed from the works of both biologists and engineers, studying the behavior of flying insects and the aerodynamics of flapping flight. With this new model, hovering hinged plates are used to study the effects of passive deflection on aerodynamic performance using two-dimensional Direct Numerical Simulations (DNS) at low Reynolds numbers (Re). The hinge is modeled as a torsional spring at the leading edge, where prescribed motion is applied. The influence of forced-to-natural frequency ratio (hinge stiffness) and stroke-to-chord ratio (leading edge kinematics) are studied, to explore the effects that either has on aerodynamic performance. Parameters are chosen from inspiration given by both insects and birds. The influences of leading edge kinematics give rise to the notion that performance improves with stroke amplitude across hinges of all stiffness. Hinge stiffness is determined to drastically affect the angle of attack at midstroke at small stroke amplitudes, as well as the behavior at stroke reversal for all kinematics. By tailoring the leading edge kinematics and the hinge stiffness, the angle of attack through the stroke and pitch rate at stroke reversal can be adjusted to promote the wake capture mechanism, and to form a stronger downwash, effectively improving the aerodynamic performance of the flapping plate. The results of this study are used to suggest a set of parameters that would be favorable for use in the conceptual hovering MAV design.

TABLE OF CONTENTS

Page

INTRODUCTION 1

BACKGROUND 7

NUMERICAL METHODS 11

Fluid Governing Equations 12

Body Governing Equations 13

Performance Metrics 15

Computational Setup 16

Preliminary Work with PICAR3D 22

RESULTS AND DISCUSSIONS 26

General Performance 26

Stroke Amplitude Effects 30

Frequency Ratio Effects 34

Design Space Exploration 39

CONCLUSIONS 46

FUTURE WORK 49

APPENDIX A 51

REFERENCES 56

LIST OF FIGURES

Page

Figure 1: 3D Finite AR flapping wing transferred to 2D 7

Figure 2: Flapping motion diagram 13

Figure 3: Fluid domain boundary conditions..... 18

Figure 4: Fluid domain schematic 19

Figure 5: Parametric study and connection to nature's flyers 22

Figure 6: Geometrical parameters of the closed wake..... 24

Figure 7: Wake measurement comparisons 24

Figure 8: Steady-state wake comparison 25

Figure 9: Vorticity contour snapshots for $A_x/c = 3$, $\omega_f/\omega_n = 1/6$. (a) t/T = 3.0, (b) t/T = 3.125, (c) t/T = 3.25, (d) t/T = 3.375, (e) t/T = 3.5, (f) t/T = 3.625, (g) t/T = 3.75, (h) t/T = 3.875, and (i) t/T = 4.0 27

Figure 10: Cycle-averaged v-velocity contour for $A_x/c = 3$, $\omega_f/\omega_n = 1/6$ 29

Figure 11: Cycle-averaged v-velocity contour for $A_x/c = 2$, $\omega_f/\omega_n = 1/6$ 31

Figure 12: Stroke amplitude effects on instantaneous C_D and C_L for $\omega_f/\omega_n = 1/6$..... 32

Figure 13: Stroke amplitude effects on vorticity contours for $\omega_f/\omega_n = 1/6$. (a-c) $A_x/c = 3$ and (d-f) $A_x/c = 4$. (a, d) t/T = 1.1, (b, e) t/T = 1.3, (c. f) t/T = 1.6..... 33

Figure 14: Cycle-averaged v-velocity contour for $A_x/c = 3$, $\omega_f/\omega_n = 1/3$ 34

Figure 15: Frequency ratio effects on instantaneous C_D and C_L for $A_x/c = 3$..... 35

Figure 16: Frequency ratio effects on vorticity contours for $A_x/c = 3$, (a-c) $\omega_f/\omega_n = 1/4$ and (d-f) $\omega_f/\omega_n = 1/5$. (a, d) t/T = 1.1, (b, e) t/T = 1.2, (c. f) t/T = 1.3. 37

Figure 17: Frequency ratio effects on angle of attack for small A_x/c ($A_x/c = 2$)..... 38

Figure 18: Cycle-averaged midstroke angle of attack for various stroke to chord and frequency ratios. (a) Variation of stroke amplitude and (b) frequency ratio..... 39

Figure 19: Cycle-averaged C_D comparison for various stroke to chord and frequency ratios. (a) Variation of stroke amplitude and (b) frequency ratio..... 40

Figure 20: Cycle-averaged C_L comparison for various stroke to chord and frequency ratios. (a) Variation of stroke amplitude and (b) frequency ratio..... 41

Figure 21: $C_{D,RMS}$ comparison for various stroke to chord and frequency ratios. (a) Variation of stroke amplitude and (b) frequency ratio..... 42

Figure 22: $C_{L,RMS}$ comparison for various stroke to chord and frequency ratios. (a) Variation of stroke amplitude and (b) frequency ratio..... 43

Figure 23: Cycle-averaged lift-to-drag ratio comparison for various stroke to chord and frequency ratios. (a) Variation of stroke amplitude and (b) frequency ratio..... 43

Figure 24: Cycle-averaged C_{PW} comparison for various stroke to chord and frequency ratios. (a) Variation of stroke amplitude and (b) frequency ratio..... 44

Figure 25: Cycle-averaged η_{aero} comparison for various stroke to chord and frequency ratios. (a) Variation of stroke amplitude and (b) frequency ratio..... 45

Figure 26: Unstructured surface triangular mesh diagram 54

LIST OF TABLES

Page

Table 1: Leading edge kinematics observed in nature 8

Table 2: Wing frequency ratios observed in nature 10

Table 3: Fluid domain dimensions 19

Table 4: Grid independence results 20

Table 5: Parameter choice for kinematics and hinge model 21

Table 6: Parametric study results 51

NOMENCLATURE

A_x	Leading edge stroke amplitude in x-direction (m)
Θ	Deflection angle (deg)
C_L	Lift coefficient
C_D	Drag coefficient
$\overline{C_L}$	Cycle-averaged drag coefficient
$\overline{C_D}$	Cycle-averaged lift coefficient
c	Chord length of plate (m)
h	Thickness of plate (m)
k	Torsional spring stiffness (N/m)
J	Moment of Inertia of plate (m^4)
ω_f	Forced frequency of plate motion
ω_n	Natural frequency of plate
Re	Reynolds number
ν	Kinematic viscosity of fluid (m^2/s)
St	Strouhal number
$\overline{C_L}/\overline{C_D}$	Cycle-averaged lift-to-drag ratio
U	Characteristic speed (m/s), based on maximum leading edge speed
θ	Deflection angle of hinged plate
ρ_s	Density of body (kg/m3)
ρ_f	Density of Fluid (kg/m3)
$\vec{F}_G$	Net body force on plate (gravity and buoyancy effects) (N)

$\vec{F}_A$	Aerodynamic force on body surface (N)
τ_G	Torque at hinge from gravitational force and buoyancy (Nm)
τ_C	Torque at body center of mass (Nm)
τ_H	Torque supplied to leading edge (Nm)
$\vec{V}_G$	Plate velocity at mass center,
l	Distance from plate mass center to hinge location
AR	Aspect Ratio
L	Distance from lee-side of plate to edge of wake
a	Distance from lee-side of plate to core of wake
b	Distance between leading and trailing edge cores of wake
α	Angle of attack (AOA), measured from horizontal
$\alpha_{midtsroke}$	Angle of attack at midstroke
C_{PW}	Instantaneous input power coefficient
$\overline{C_{PW}}$	Cycle-averaged input power coefficient
$F_{H,x}$	Hinge force in x-direction
P_{tr}	Translational power
P_{rot}	Rotational power
F_L	Lift (vertical, aerodynamic) force on plate
F_D	Drag (horizontal, aerodynamic) force on plate
M_R	Mass ratio between plate and surrounding fluid
η_{aero}	Aerodynamic efficiency

ACKNOWLEDGEMENTS

I would like to thank my adviser, Dr. Haibo Dong, for his support during this project and all previous ones. I have had the pleasure of working with him since my first year of undergraduate studies and because of the opportunities he has given me, I have learned and explored problems and concepts that, prior to our meeting, I did not know existed. He has instilled trust in my abilities and provided every resource needed to explore any problem I have worked on. Dr. Hui Wan and everyone from Dr. Dong's research group at WSU have helped me to trouble shoot any problems I have had with PICAR3D and have provided countless suggestions and new ideas in regards to my work.

I would like to thank Dr. Michael Ol and Dr. Kenneth Granlund for their frequent suggestions, from which, this body of work has improved tremendously. Their perspectives were not only fresh and expert, but their commentary on the matter always seemed to lighten the mood. I would also like to thank Dr. Philip Beran for his support during the past two summers. Working with him and his team allowed me to hone and develop my skillset, expanding my knowledge of CFD and introducing me to experiment design and optimization methods.

Finally, I would like to thank my friends and family. My parents were instrumental in my interest in science and math, which brought me into the field of engineering. I would also like to thank Kayla Hamilton for her relentless optimism and continued support of both my research and my ambitions. Oh, and our dog, Gracie, who remained by my side every night I spent working on this project and manuscript.

Thank you all

INTRODUCTION

With the growing demand for micro air vehicles (MAVs), capable of performing agile maneuvers and possessing the ability to hover in place, many designs have been manufactured and studied, in the hopes of creating a well-rounded, robust vehicle. These designs often gain inspiration from nature, where insects and birds have perplexed observers with their adept flight skills for millennia, primarily some species' ability to hover. Modeling a hovering MAV after nature requires knowledge of flapping flight, which has been in extensive development in both the biology and engineering research communities. Both fields recognize the importance of deformation in the wings and the inherent flexibility within the wing structure. To this end, researchers have made efforts in studying both the kinematics involved in hovering flight, and the effects of both flexibility and rotation interaction between the wing and surrounding fluid.

Many works have been made in regards to studying the forces generated in hovering flight. One such significant work not only isolated a set of parameters which are ideal for hover, but also discussed and explored the implications of modeling a 3D flapping wing with a 2D simulation. (1) compared both computational and experimental results on force for wings undergoing hovering flight at low Reynolds numbers. They compare the validity of 2D results to 3D and discuss the implications of studying one over the other. They suggest that in the range of stroke amplitudes studied, A_x/c =3 to 5, force had little dependence on amplitude. The greatest dependence was on the phase between stroke angle and angle of attack, a key component in affecting the stroke reversal. This research also concludes a set of kinematics for both pitching and plunging

that yielded ideal force production for hover. They use the velocity and acceleration profiles of the wings in accordance with the calculated and measured forces on the wing to explain the 3D effects. In most cases, 2D calculations under predict the 3D forces, as aspect ratio effects are neglected. However transient force phenomena are captured in the 2D results, and thus, are a good predictor for 3D flapping. This is especially true for cases where flow on a flapping wing remains attached throughout the majority of the stroke.

As most micro air vehicle (MAV) designs have begun to look to nature for inspiration, studying the effects of flexible flapping wings, such as those found in insects and birds, has become more appealing. As the bulk of biological wings are deformed passively, little is known as to what role these chord-wise deformations in the wing structure play in promoting aerodynamic performance. To this end, (2) performed studies on the effects of chord-wise flexibility on hovering kinematics of flapping wings using a direct numerical simulation (DNS) of the Navier-Stokes equations coupled with the dynamics of the wing.

A hovering wing was modeled in 2-dimensions as a two or three rigid link system, joined at a location along the chord wise direction by a hinge, where the hinge force is modeled as a torsion spring. The rigid links are represented by an elliptical cross-section and the leading rigid section of the wing is driven by prescribed hover kinematics, with the trailing sections allowed to interact and deflect passively with the surrounding fluid. To provide better insight into the critical factors used to determine aerodynamic performance in flexible wings, heaving amplitude is varied between 0.5 and 6 chord lengths, chord-wise position of the point of rotation varies between 0 and 50% chords

distance from the leading edge, pitching and heaving phase lag varies from 0 to 70^{o}, and pitching amplitude is varied from 0 to 45^{o}.

It was determined that wing flexion allowed for lower power consumption for driving the wing when compared with fully rigid wing sections, but, at large heaving amplitudes, caused a reduction in performance due to premature detachment of leading-edge vortices (LEVs). Sensitivity of lift generation to pitch-heave phase difference was reduced with added flexibility, due to the stored energy within the spring-hinge being released at stroke reversal, resulting in a much stronger downwash. This evacuation of vorticity from the near field region surrounding the motion of the plate accommodates the generation of a new LEV at stroke reversal, generating higher circulatory lift.

Extensive work has been made in studying the effects of hinge stiffness for similar physical models. (3) looked at the effects of Reynolds number, hinge stiffness and grid resolution on a two-link plate with a torsional spring hinge located at the mid-chord location. They used a coupled fluid and body dynamical system where the fluid forces were governed by the NS equations. The upper-section was prescribed with fixed motion based on the ideal hover kinematics determined by (1) and the trailing section was allowed to interact with the flow. With only one unknown variable, trailing edge deflection angle, a non-dimensional parameter was chosen to govern the hinge stiffness, forced to natural frequency ratio. They determined that the use of this chord-wise flexibility could enhance the aerodynamic performance via the lift to drag ratio and this peak in performance improvement occurs at a frequency ratio of 1/3, which coincides with a non-linear resonance in the system. At this peak performance location, wake capture was enhanced at all Reynolds number due to the strength of the flow around the

wing at stroke reversal. Lift per unit power also improved with Reynolds number. They pose the question of which kinematics is best suited for performance, why does the performance increase at this particular non-linear resonance, and would performance also increase at a point of linear resonance.

The previous work had not addressed freely rotating plates with no hinge resistance or the effects of hinge location along the chord. (4) used the equations of motion with no spring at the hinge in tandem with an accurate DNS tool to simulate freely rotating hinge plates. To prevent the unrestricted plate from detrimentally rotating on it during the flapping, limiters are put in place, restricting the deflection of the free section. The leading edge is driven sinusoidally and the effects of stroke amplitude are also explored. For a leading edge hinge, performance via the lift to drag ratio improved with an increase in stroke amplitude, and for very small stroke amplitudes, the lift can be very small and sometimes negative. A hinged plate also outperforms a rigid prescribed plate when the hinge is moved to ¾ the chord length. It is also noted that increasing rotational freedom does not necessarily improve performance directly; however, tailoring the rotational freedom and kinematics can promote better lift production and lower input power consumption.

An essential component to flapping flight is the interaction of the wing and fluid at the point of stroke reversal. (5) studied the effects of pitch change at the moment of reversal for insect flight. They studied tethered dragonflies, hovering fruit flies, hovering hawkmoths, and a simplified form of the dragonfly hovering kinematics. The aim of their study centered on whether the pitch reversal was active or passive. Through calculations of rotational power about a pitching axis, it was determined that the fluid assisted rather

than hindering the reversal. For such an essential component of lift stability and generation to be passive, suggests that a flapping wing MAV could control the pitching mechanism during flapping with a passive component, such as a torsional spring, to effectively improve performance, without adding complexity to either the controls or manufacturing aspects of the MAV design.

The works mentioned above suggest that for a simplified hovering MAV design, modeled after insects or birds capable of hover, there are several factors that should be considered in the design: wing translation and rotation, flexibility in the wing, and behavior at stroke reversal. Capitalizing on simplicity, a good design could be made with all passive components, where engaging the flapping wing controls all aspects that are important to flight performance. Translation will be dictated by linkages, rotation will be passively governed by a component in the wing, and the behavior at stroke reversal will be controlled by these two design principles.

In this work, this simplified MAV design is chosen, and deformable flapping wings are modeled as a hovering rigid membrane plate with prescribed leading edge kinematics. A torsional spring, whose stiffness is governed by a ratio of forced-to-natural frequency, is placed at the leading edge and driven sinusoidally with the deflection of the membrane determined by its interaction with the surrounding fluid. The effects of hinge stiffness and stroke amplitude are studied and aerodynamic performance is discussed therein. While hovering is the major impetus of this work, it is noted that this work could be adapted to study other flight modes, such as takeoff, cruising, and quick yaw turns, all of which are observed in nature and a desired attribute for most MAVs. The subsequent section discusses the related MAV design and parameters chosen for this study.

BACKGROUND

In the interest of designing a relatively easily manufactured MAV, a leading edge driven flapping mechanism is to be modeled. Within the leading edge joint, the relatively rigid wing is attached to the actuating mechanism and allowed to rotate in a pitching manner relative to the flapping motion.

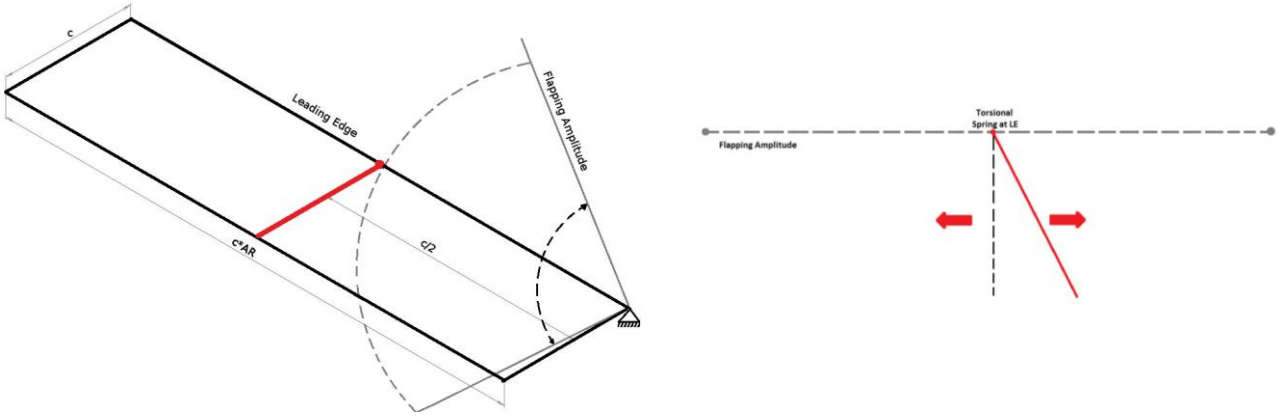

Figure 1: 3D Finite AR flapping wing transferred to 2D

While some conceptual MAV designs have had these free-to-rotate concepts included in the wing joint, with fixed limiters restricting the range of rotation, to create a more realistic rotational joint, the freely rotating hinge is replaced with a torsional spring that will provide resistance in flapping, which will affect the angle of attack during the stroke. Little to no research has been made on a one-link plate with this sort of flapping mechanism in mind. To this end, an experiment is designed, taking into account key features of design, such as the appropriate kinematics for such a device, the desired flight maneuver for the MAV or the spring stiffness selection.

A MAV should have the capability to take off and maneuver on its own, but the most interesting maneuver that MAVs hope to be able to perform is hovering. If an MAV

can hover in one location it will allow for surveillance and reconnaissance of an area. While the kinematic profile can take on many trajectories, in traditional hovering studies on insects, a simple sinusoidal plunging trajectory is chosen. To keep in accordance with this tradition, this work uses the same.

This leaves two major design parameters: range of motion and spring stiffness. From the works of (3) and (4) we see that hinge stiffness can be modeled through the frequency ratio and the range of motion can be controlled via the dimensionless stroke amplitude. Selection of these parameters can prove challenging as there is a wide range of parameters that can be chosen. To gain a better understanding of what realistic values for these parameters can be, insight is gathered from a review of the dimensionless stroke amplitudes employed by some of nature's greatest flyers in all aspects of flight, not only hover, summarized in Table 1.

Table 1: Leading edge kinematics observed in nature

Species	**Beating Frequency [Hz]**	**AR**		**Stroke Amplitude [°]**		**A_x/c (at midspan)**		**Source**
Dragonfly (*Anax parthenope julius*)	26.5	*FW*	10	*FW*	72	*FW*	6.28	(6)
		HW	7.8	*HW*	52	*HW*	3.53	
	29	*FW*	10	*FW*	50	*FW*	4.36	
		HW	7.8	*HW*	52	*HW*	3.53	
	27	*FW*	15.7	*FW*	76	*FW*	10.41	
		HW	9.3	*HW*	68	*HW*	5.5	
Fruit fly *(Drosphila melanogaster*)	200	*W*	2.4	*W*	148	*W*	3.12	(7)
Bumblebee (*Bombus terrestris*)	150	*W*	6.6	*W*	120	*W*	6.93	(8)
Hawkmoth (*Manduca sexta*)	25	*W*	5.3	*W*	115	*W*	10.60	(9) (10)
Hummingbird (*Lampornis clemenciae*)	23	*W*	8.2	*W*	148	*W*	10.66	(11) (12)

Further review of parameters found in nature reveals that extensive studies have been performed on the stiffness of some insects such as dragonflies and damselflies. By using the observed beating frequency of the flapping wings on these various species and the experimentally determined natural frequencies of those wings, the frequency ratio at which insect wings operate under is summarized in Table 2. The data for which was adopted from (13) and (14).

Table 2: Wing frequency ratios observed in nature

Species	**Mass [mg]**	**Beating Frequency [Hz]**	**Natural Frequency [Hz]**	ω_f/ω_n
Lesser Emperor Dragonfly (*Anax parthenope julius*)	670	27	75	0.360
			120	0.225
Damselfly (*Cercion calamoum calamorum*)	27	41	133	0.308
Aka-tombo Dragonfly (*Sympetrum baccha matutinum*)	191	31	67	0.463
Damselfly (*Calopteryx atrata*)	245	15	48	0.313

Studying the realm of known operating conditions of natural flyers will serve as a great starting point of investigation for an ideal combination for a conceptual MAV design. It is with this information that the design parameters for this study are chosen and discussed in the next section of this work.

NUMERICAL METHODS

For this work, a non-commercial computational fluid dynamics tool, PICAR3D, is employed and the outputs of such (pressure and velocity fields) are used to calculate the forces acting on the flapping plate. From these quantities and other subsequent metrics, performance is analyzed and the parameter effects are discussed in later sections. This section outlines a summary of PICAR3D, numerical methods used in the simulations, computational parameters used, and preliminary studies that were performed with PICAR3D.

For this research, a finite-difference-based approach for computing flows with moving immersed boundaries on fixed Cartesian grids is employed. The incompressible Navier-Stokes equations are discretized using a cell-centered non-staggered (collocated) mesh arrangement of the primitive variables (u_i , p). In addition to the cell-center velocities (u_i), the face-center velocities (U_i) are computed. The time-integration is based on the fractional step method of Van-Kan (15). In the current solution procedure, the convective terms are represented using an explicit second-order Adams-Bashforth scheme; whereas the diffusive terms are modeled with an implicit Crank-Nicolson procedure. The spatial derivatives have been discretized with a second-order accurate central difference scheme. A semi-coarsening multigrid solver is invoked for the Pressure Poisson Equation. In addition to the high-fidelity fluid solver, a new feature is added into the program, allowing for implicit coupling of body equations of motion. Thus, the solver now has flow-body interaction capabilities directly within.

Fluid Governing Equations

PICAR3D uses the incompressible Navier –Stokes (NS) equations to simulate the fluid interactions. These equations, continuity and x and y momentum, are given in tensor notation in (1).

$$\frac{\partial u_i}{\partial x_i} = 0 \, , \frac{\partial u_i}{\partial t} + \frac{\partial u_i u_j}{\partial x_j} = -\frac{\partial p}{\partial x_i} + \frac{1}{R_e}\frac{\partial^2 u_i}{\partial x_j x_j} \quad (1)$$

Here, u_i (i = 1,2) is the velocity components, and p is the pressure. The NS equations are solved using a finite-difference based, Cartesian grid, immersed boundary method. A second-order central difference scheme in space is employed and a second-order accurate fraction-step method for time integration is used as well. More information on this DNS solver can be found in (16) and (17; 18).

Reynolds number (Re) is crucial in dictating the characteristics of the flow field. Given by (2), where the characteristic speed in open flow (hover conditions) is chosen to be the maximum leading edge velocity. This value is easily determined by the first temporal derivative of the prescribed LE kinematics given in (7). The Re is set to a fixed value for the majority of cases and the maximum leading edge velocity is held constant.

$$\mathrm{Re} = \frac{Uc}{\nu} \quad (2)$$

This allows for a fair comparison of various kinematic profiles on a non-dimensional basis.

Body Governing Equations

In general, the equations of motion for a rigid body, accounting for translation and rotation, are given by (3) and (4).

$$\vec{F}(t) = m\frac{d\vec{V}_C}{dt} \tag{3}$$

$$\tau_c = \boldsymbol{J}\cdot\ddot{\Theta} + \dot{\Theta}\times\left(\boldsymbol{J}\cdot\dot{\Theta}\right) + K\boldsymbol{I}\Theta \tag{4}$$

The total force $\vec{F}(t)$ is comprised of corrected gravitational force $\vec{F}_G$, which accounts for buoyancy, surface aerodynamic force ($\vec{F}_A$), and hinge ($\vec{F}_H$). The net torque $\vec{\tau}_C(t)$ is comprised of aerodynamic torque ($\vec{\tau}_A$) and external torque and acts at the mass center of the plate. *K* is the spring constant and the aerodynamic force and torque are obtained via the surface integration of pressure *p* and viscous stress tensor $\boldsymbol{\sigma}$, as given by (5) and (6).

(a)

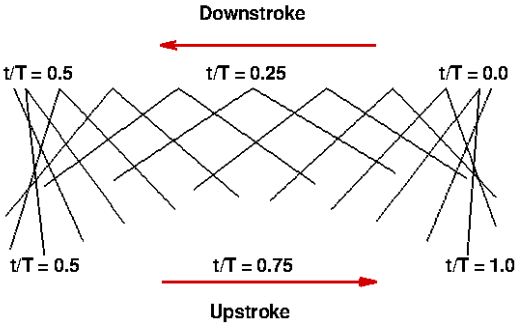

(b)

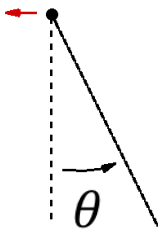

Figure 2: Flapping motion diagram

$$\vec{F}_A = \int_s (\boldsymbol{\sigma}\cdot\vec{n} - p\vec{n})ds \tag{5}$$

$$\vec{\tau}_A = \int_s (\boldsymbol{\sigma}\cdot\vec{n} - p\vec{n})\times\vec{r}ds \tag{6}$$

The hinged plates rotate and translate about the leading edge (LE) in the x-y plane, shown in Figure 2. The prescribed plate motion is sinusoidal, in the horizontal, and stationary with respect to the vertical direction, given by (7). The deflection angle, θ, is determined

from the interaction between the body and the surrounding fluid via the coupling between (3) and (4) and the fluid solver.

$$x(t) = \frac{A_x}{2}\cos(\omega_f t), \quad y(t) = 0 \tag{7}$$

The implicit methodology used in coupling the body and fluid is described in greater detail in (4).

The Strouhal number (St) is often used to describe oscillating flow mechanism such as vortex shedding. However, for flapping flight studies, the Strouhal number is often characterized by two definitions, the first as a ratio of flapping velocity to forward flight velocity, but in hover, the body forward flight velocity is always zero because the body is stationary. For a more useful Strouhal number in hovering flight, another definition is employed, given by (8). This is often referred to in flapping flight literature as the reduced frequency (19). Once again, the reference velocity is chosen as the maximum leading edge velocity, which, in turn, defines St as the inverse of $(\pi A_x)^{-1}$.

$$\mathrm{St} = \frac{fc}{U} \tag{8}$$

Another important characteristic governing this simulation is the effects of hinge stiffness. To do this, a frequency ratio of force-to-natural frequency (ω_f/ω_n) is used. The equations for such are given by (9) and (10). In this case, the hinge stiffness, k, is determined by the plates geometry, via the moment of inertia, J, and the force frequency of the plate. The convention of use for this parameter was observed in many structural dynamics papers referring to the material properties of insect wings as well as (3). The forced-to-natural frequency ratio is used to balance the inertial loading with the stiffness of the hinge.

$$\omega_f = 2\pi f \tag{9}$$

$$\omega_n = \sqrt{k/J} \tag{10}$$

One particularly important dependent variable that should be taken into consideration when discussing performance of a flapping wing is the required input power that should be supplied to the wing to provide the wings motion which achieves the calculated lift and drag. For this application, the input power is calculated by assuming that all power is supplied only at the leading edge, where the torsional spring is located, and that the force is only supplied in the horizontal direction. The force supplied to the leading edge, $F_{H,x}$, as well as the leading edge torque, τ_H, are responsible for continuous flapping. Treating the plate as a single link, the force $F_{H,x}$ and torque τ_H are given by (11) and (12), respectively.

$$F_{H,x} = m\frac{d\vec{V}_{G,x}}{dt} - F_{A,x} \tag{11}$$

$$\tau_H = J\ddot{\theta} - \tau_G - \tau_A - m\ddot{x}l \tag{12}$$

Performance Metrics

To measure the input of these two actions, power is treated as two components: translational (P_{tr}) and rotational (P_{rot}), which are given by (13) and (14), respectively.

$$P_{tr} = F_{H,x}\dot{x} \tag{13}$$

$$P_{rot} = \tau_H\dot{\theta} \tag{14}$$

From the two power components, input power coefficient is defined by the power associated with dynamic pressure. The power is non-dimensionalized, into coefficient form, using the maximum leading edge velocity, determined by the temporal derivative

of the prescribed LE kinematics. It should be noted, that the cycle-averaged input power, $\overline{C_{PW}}$, is calculated from positive power only. This definition is the same as used by (20), (3), and (4), which is given by (15).

$$C_{PW} = \frac{P_{tr}+P_{rot}}{\frac{1}{2}\rho_f U^3 c^2} \tag{15}$$

Using conventional definitions of aerodynamic force, determined from the integration of surface pressure on the plate and the orientation of plate, force coefficients are given by (16) and (17).

$$C_L = \frac{2F_L}{\rho_f U^2 c} \tag{16}$$

$$C_D = \frac{2F_D}{\rho_f U^2 c} \tag{17}$$

The cycle-averaged lift-to-drag ratio is used as a metric of aerodynamic performance in accordance with the ratio of lift to power, given as the aerodynamic efficiency, shown in (18).

$$\eta_{aero} = {C_L}/{C_{PW}} \tag{18}$$

From these methods and metrics, the leading edge, torsional spring hinge connected plate is simulated, using the details outlined in the following subsection, and the associative effects on aerodynamic performance are simulated in the results section of this manuscript.

Computational Setup

Due to the methodologies involved in PICAR3D, a Cartesian grid fluid domain is used to represent the fluid medium, which, in this case, is air. The immersed boundary method uses techniques that allow for accurate flow calculations of all sorts, particularly

of interest is the simulation of moving boundaries that have the capability to perform highly adept maneuvers, or in some case have the capability to deform, such as that of an insect wing. More information on this algorithm is found in (16). It is under these restrictions, that the immersed boundary is advantageously employed for simulating a flapping wing of zero-thickness (membrane).

As previously mentioned, Cartesian grids are used for the fluid domain. For the 2D plane, after non-dimensionalizing the wing, the domain is chosen to be 30c x 30c, which has been noted in many literatures as a sufficient enough domain size for open flow hovering conditions. For a Navier-Stokes representation of the flow, boundary conditions are chosen at top, bottom, left, right, front and back (in and out of plane) for both velocity and pressure terms. Because the motion is hovering, it is assumed that there is no incoming flow at any bounds and that the boundaries are sufficiently far away from the plate's motion. When the boundary is moved far away from the motion of the plate, it is assumed that there is no change in the flow with respect to direction at the bounds. To this end, Neumann boundary conditions are applied for both velocity and pressure (set to zero) for representing a zero gradient of flow and pressure at the bounds. This is a common representation of hover as found in many similar works (17). The diagrams of the boundary conditions are found in Figure 3.

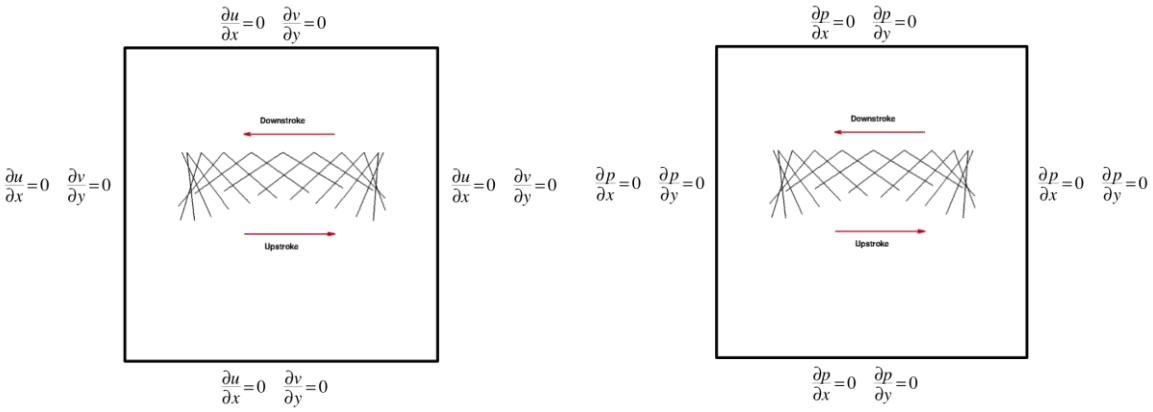

Figure 3: Fluid domain boundary conditions

Because the flow domain is relatively large, the Cartesian grids are split into two regions, a dense, uniformly spaced region, and a stretching region that extends to the boundaries. It has been shown that the use of stretching grids was suitable in the far-field region and a more uniform higher resolution can be used in the near-field region. The schematic showing the formation of the fluid domain is shown in

Figure 4. The dense region is symmetric about the global domain and the aspect ratio of the grids is set as close to unity as possible. The pressure-Poisson step of PICAR3D is solved using a geometric multigrid method (using a modified SIP smoother) and because of this, the domain is chosen to have a total number of grids in either direction as close as possible to a $(2^N - 1)$ relationship. Convergence efficiency is drastically improved by having a domain that is highly divisible by two. This is due to the nature of the multigrid method, where residuals calculated on a fine domain, are applied to a coarse domain successively and projected back to a fine domain, effectively speeding up the convergence of a Laplacian equation such as the pressure-Poisson equation.

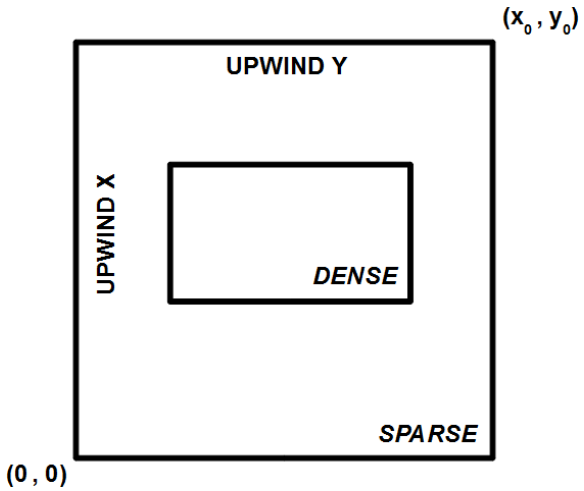

Figure 4: Fluid domain schematic

Because the range of motion for the hovering plate differs based on the stroke amplitude that is chosen, different domains are selected for each stroke amplitude and the parameters and dimensions for each are summarized in **Error! Reference source not found.**.

Table 3: Fluid domain dimensions

A_x/c	Dense		Sparse - Upwind, Downwind		Total Resolution	Total Grids
	Dimensions	Grids	X	Y		
0.5	2.5 x 5	240 x 480	17 , 15	17 , 15	273 x 513	140,049
1	3 x 5	288 x 480	17 , 15	17 , 15	321 x 513	164,673
2	4 x 5	384 x 480	17 , 15	17 , 15	417 x 513	213,921
3	5 x 5	480 x 480	17 , 15	17 , 15	513 x 513	263,169
4	6 x 5	576 x 480	17 , 15	17 , 15	609 x 513	312,417
5	7 x 5	672 x 480	17 , 15	17 , 15	705 x 513	361,665
6	8 x 5	768 x 480	17 , 15	17 , 15	801 x 513	410,913
10	13 x 5	1248 x 480	17 , 15	17 , 15	1281 x 513	657,153

In general, each of the domains uses a relationship of 96x96 grids for a 1c x 1c area within the dense domain and a total of 32 stretching grids in either direction of the

far-field region. From running successively refined domains in both the near- and far-field regions of varying dimensions, with less than five percent change in force production and no observable change in velocity fields, it was determined that these domains were adequate for simulating these hovering hinged plates. Results of such a comparison are summarized in Table 4. Similar grid domains and techniques are employed in (4).

Table 4: Grid independence results

A_x/c	ω_f/ω_n	C_D			C_L		
		3c Domain	5c Domain	% Difference	3c Domain	5c Domain	% Difference
3	0.125	2.1730	2.1212	-2.3852	1.0470	1.0154	-3.0181
3	0.143	1.9030	1.9105	0.3941	1.0850	1.0957	0.9862
3	0.167	1.5752	1.5716	-0.2304	1.0623	1.0613	-0.0957
3	0.200	1.1540	1.1535	-0.0433	0.9290	0.9295	0.0560
3	0.250	0.7490	0.7490	0.0000	0.6639	0.6640	0.0151
3	0.333	0.3710	0.3709	-0.0270	0.2620	0.2619	-0.0458

It is very important to choose parameters that are found in nature as well as within a feasible region of design. As shown previously in Table 1 and Table 2, insects have both a variety of frequency ratios and kinematic profiles. To this end, a wide span of frequency ratios were selected to cover the spectrum from very loose hinges (1/3) to very stiff hinges (1/8). This range encapsulates many insect species and should be achievable in design as well. The choice of dimensionless stroke amplitude ranges from 0.5 to 6 and some specialty cases of 10 chords. This will cover many species from fruit flies and dragonflies all the way up to hummingbirds. The summary of parameter levels is shown in Table 5.

Table 5: Parameter choice for kinematics and hinge model

Parameter	Levels						
ω_f/ω_n	1/3	1/4	1/5	1/6	1/7	1/8	--
A_x/c	0.5	1	2	3	4	5	6

The Reynolds numbers in the simulations are all 188.4, which was chosen from within the feasible range for insect flights and also falls within the acceptable tolerance for DNS solvers such as this one. To increase the Reynolds number beyond 1000 with DNS, the mesh refinement in the near-field region would have to be much finer to capture the smaller eddies forming. For a moving body such as this one, the local mesh refinement is currently not feasible for a study of this magnitude, as that resolution is computationally too costly for a 2D design study. In our study, the mass ratio, given by (19) is 0.2.

$$M_R = \frac{\rho_s \, h}{\rho_f \, c} \tag{19}$$

The mass ratio of a cranefly and dragonfly is estimated to be 0.34 (21) and 0.8 (13) respectively. Thus, the wing in the current study is light and most analogous to a cranefly. The infinitely thin membrane assumption is made based on the case of a density ratio of 20, the ratio of thickness to chord length $\frac{h}{c} = 0.01$, which can be modeled as a membrane. Assuming the density ratio between solid and fluid increases and the wing material in air becomes denser, the thickness ratio further reduces, justifying the membrane assumption more easily.

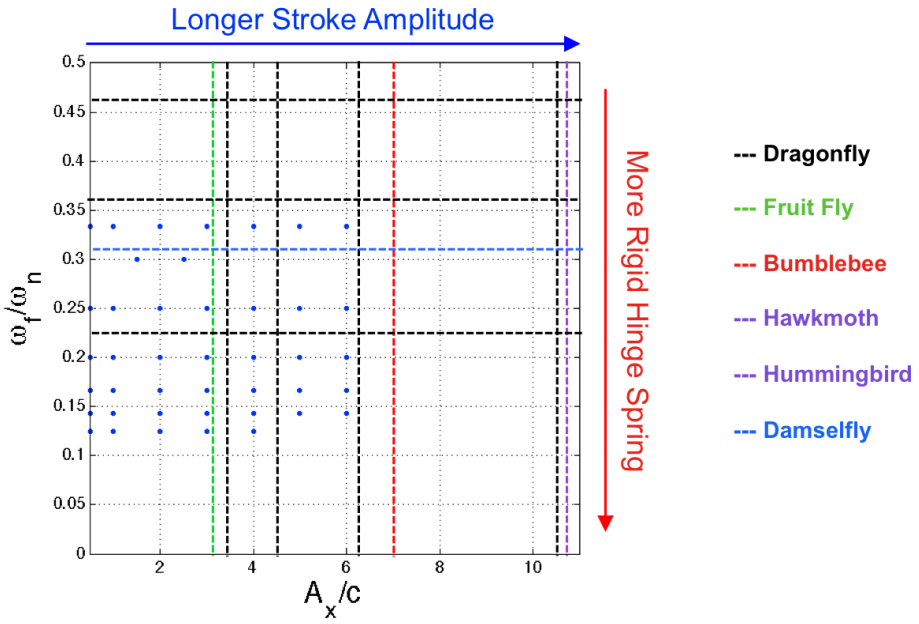

Figure 5: Parametric study and connection to nature's flyers

To further elucidate the connections between the cases explored in this study and realistic parameters of some of nature's best flyers, an overlay of parameters and cases are shown in Figure 5. The horizontal dashed lines represent the cited operating ranges of frequency ratio for that species, but these citations do not measure the kinematics of the species. The vertical dashed lines represent the cited kinematics of various species, but do not claim a particular range of frequency ratios. The dashed lines together represent a set of possible relevant parameters found in nature. The solid blue dots show parameters chosen for simulation in this work. The results of such are shown in later sections of this document.

Preliminary Work with PICAR3D

While PICAR3D is well validated(16) and has been used many times over for publications regarding bio-inspired kinematics in low Reynolds number flows

(18)(22)(23), validations were performed as a means of gaining confidence in results as well as experience with the solver. While both the accuracy of flow representation and force calculation have been made in the cited works above, further validation of the flow field calculation was made.

It is crucial for a DNS solver to accurately predict not only the force, but also the flow field structure. With an accurate representation of the flow field, connections can be made between the flow phenomena and the aerodynamics performance of the flapping wing. Connections between flow and force are fundamental in understanding fluid mechanics, especially for MAV and other aerospace applications. To this end, impulsively started (initially at rest, then suddenly moved) vertical plates are simulated at low Reynolds numbers and the flow field is analyzed. At low Reynolds numbers, a vertically inclined plate is expected to generate some disturbance in the flow and a separated vortex will emanate from the lee-side at both the leading and trailing edges of the plate. The size, shape, and position of the wake is tracked through time and compared with results obtained experimentally and numerically by (24) and (25). The wake position, size and shape measurement definitions are shown in Figure 6.

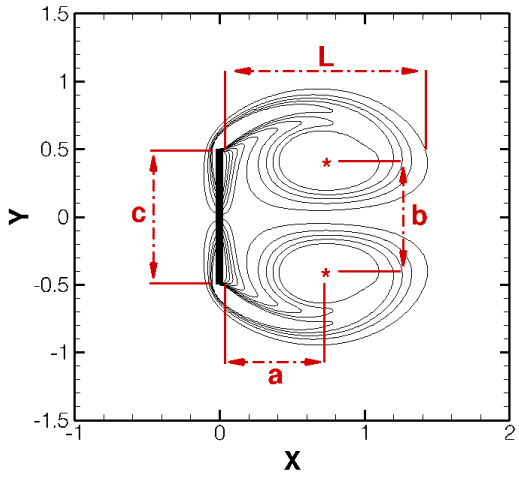

Figure 6: Geometrical parameters of the closed wake

Using PICAR3D simulations were made at a low Reynolds number (Re = 10) for a flat plate, normal to flow, set with a unity freestream velocity boundary condition at left, zero velocity gradient at right, and no slip velocity condition enforced at top and bottom bounds. The top and bottom bounds were placed to insure 20% blockage of the domain by the plate and then simulated for five convective time units. The flow field z-component vorticity was plotted periodically and measurements of the wake were made.

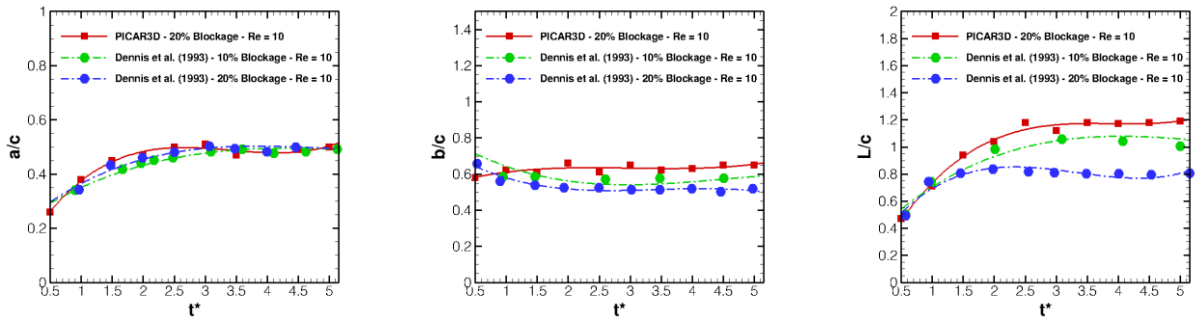

Figure 7: Wake measurement comparisons

The PICAR3D solution matched well with experimental results, shown in Figure 7, which gives more confidence in the solver's ability to capture accurate representations

of flow fields. A qualitative comparison is made between the streamlines calculated from the velocity field results of PICAR3D and experimental data from Dennis et al. where aluminum particles are present in the flow field. The comparison is made for the steady-state wake (Re = 10) between 20% blockage (computational) and 10% blockage (experimental). Figure 8 shows the overlay of streamlines (green) with the original experimental data.

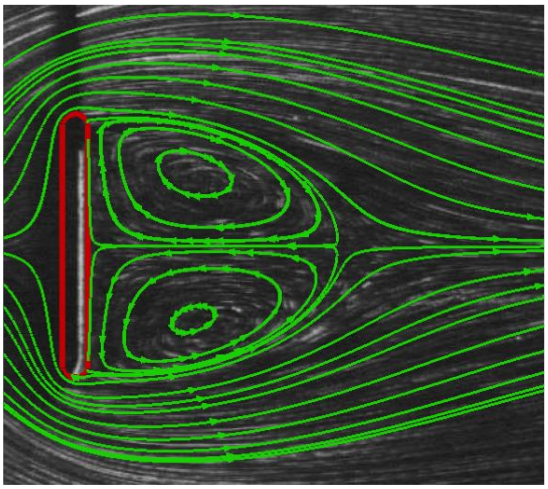

Figure 8: Steady-state wake comparison

Some possible explanations for the discrepancies between the computational and experimental results may have to do with the measurement definitions. As it is difficult to determine the exact core and length of the wake from streamlines, some error is introduced. Due to the lack of information provided by Dennis et al. it is unclear how the experimental measurements were made. Figure 8 shows an excellent correlation between the computational solution and experimentally observed wake. This validation, among many others made for previous works, suggests that PICAR3D is accurate enough to capture flow phenomena at low Re.

RESULTS AND DISCUSSIONS

After successful simulation of the previously described cases, the deflection of the plate, force on the plate and input power supplied to the plate were processed. The data has been organized into four subsections: general performance, stroke amplitude and frequency ratio effects on instantaneous force and vorticity, and a design space exploration on averaged force coefficients and input power.

General Performance

The overall progression and wake formation of the flapping foil is discussed through subsequent z-component vorticity snapshots. Figure 9 shows one particular case of $\omega_f/\omega_n = 1/6$ undergoing kinematics with $A_x/c = 3$. This case was chosen specifically as a moderate range of motion with a relatively rigid hinge spring. The plots of vorticity are shown with contour levels from -5 to 5, where red contours show clockwise rotation and blue contours show counterclockwise rotation.

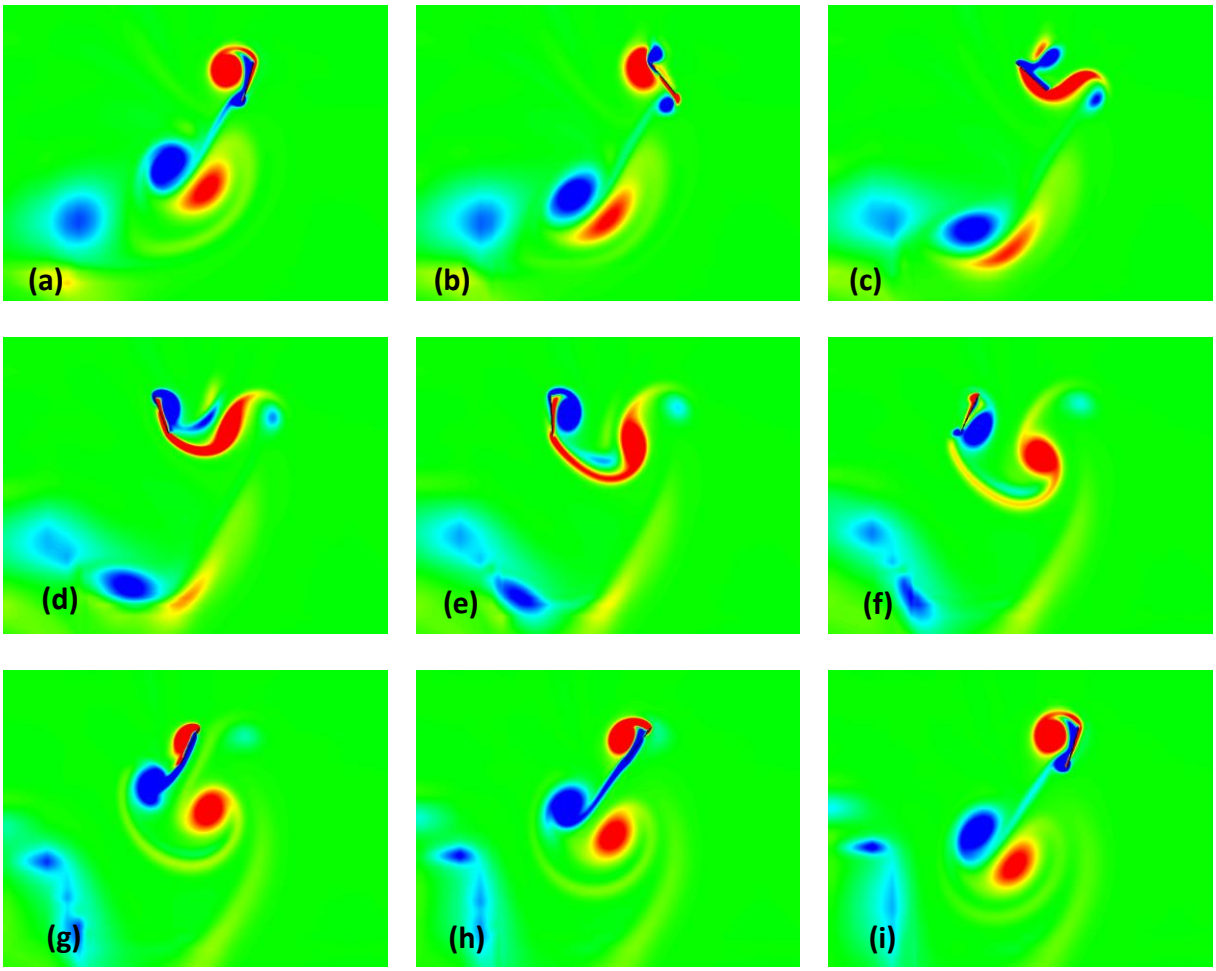

Figure 9: Vorticity contour snapshots for $A_x/c = 3$, $\omega_f/\omega_n = 1/6$. (a) t/T = 3.0, (b) t/T = 3.125, (c) t/T = 3.25, (d) t/T = 3.375, (e) t/T = 3.5, (f) t/T = 3.625, (g) t/T = 3.75, (h) t/T = 3.875, and (i) t/T = 4.0

The initial vorticity snapshot shown in Figure 9a is taken from the start of the fourth stroke cycle, at right extreme. A pair of counter rotating vortices that have been previously shed are located midway of the plates horizontal range of motion. The plate is initially inclined at a negative angle with respect to the motion of the leading edge. The torsional spring, which had been deflected in the upstroke of the previous cycle, has some stored energy, which is released at the point of stroke reversal, causing the plate to rotate faster than a freely pivoting hinge would allow. A leading edge vortex (LEV) from the

previous stroke is fully developed and detached from the plate, while a trailing-edge vortex (TEV) is forming. As the stroke progresses and the plate begins to travel away from the right extreme, the previously formed LEV is reattached to the windward side of the plate, via wake capture, and a counter-rotating LEV is formed. The previously forming TEV separates from the plate and residual vorticity is convected from the leading to the trailing edge on the lee-side of the plate.

Now at the midpoint of downstroke, Figure 9c, the plate is at its maximum velocity. The newly forming LEV is attached to the lee-side of the plate, which is responsible for the peak in lift production at midstroke. However, it is noted that the new LEV has a large diameter region where it appears to begin shedding. The reattached windward LEV is pushed to the trailing edge by the plate's motion and joined with the residual vorticity from the lee-side, now forming a new TEV. The stiffness of the spring along with the kinematics of the plate govern the deflection of the plate, for this particular choice of parameters, the plate remains a relatively high angle of attack (AOA) at midstroke, approximately 45^{o}, causing the TEV to form with a larger diameter than those observed in plates whose mid-stroke AOA was diminished.

In Figure 9d, as the stroke progresses, nearing reversal, the leading edge slows and the torsional spring begins to release energy causing the plate to rotate towards its equilibrium orientation (upright). This causes the LEV that appeared to be shedding at midstroke, to reattach to the lee-side. Upon stroke reversal, this LEV attachment will aid in wake capture, which will promote a sudden increase in lift at the start of the upstroke. The plate rotation aids in separating the TEV, ultimately pushing it into the downwash. It is observed that as hinge stiffness increased, a larger amount of energy was stored in the

torsional spring, causing the plate to rotate faster than weaker hinges (or freely pivoting plates) at stroke reversal, which, in turn, increased the downwash.

At stroke reversal, Figure 9e, the plate begins to move towards the previously formed LEV, supporting growth of a new TEV and the sudden change in direction and speed of the leading edge causes the formation of a new counter rotating LEV. As the plate moves to the midpoint of the upstroke, the LEV is attached to the lee-side of the plate once again. Comparing the LEV attachment in the up and down strokes reveals that the down stroke has better LEV attachment along the entire plate, causing the lift to have a higher peak value than in the upstroke.

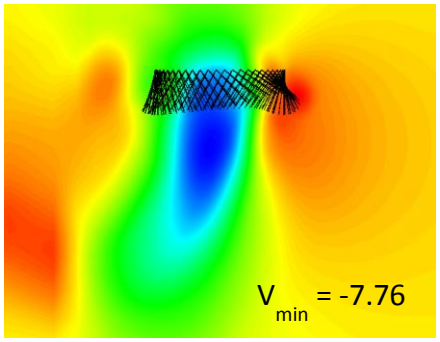

Figure 10: Cycle-averaged v-velocity contour for $A_x/c = 3$, $\omega_f/\omega_n = 1/6$

The downwash of the plate is analyzed through a cycle averaged v-velocity contour, shown in Figure 10. The velocity field is averaged using data collected over 3 flapping periods. During these three strokes, 50 velocity field snapshots are collected for each period, and then averaged to create an average velocity field. It is important to analyze this field, as it provides information about the down wash and the overall energy in the flow. Over three periods, this particular case shows that a consistent and prolonged downwash (blue contours denote negative v-velocity) forms in the center of the stroke range. The downwash favors the initial motion direction, as this is where the first vortex

is shed, causing the wake to bend in this general direction. It should be noted that the warmer (more red) colors denote a positive v-velocity (upwards). This phenomenon tends to occur outside the stroke reversal pointes, showing a clear downwash channel within the confines of the plate's motion. It should be noted that this selected case was a high-lift generating case with good overall performance metrics.

Stroke Amplitude Effects

To elucidate the effect of decreasing stroke amplitude, a case is chosen using the same frequency ratio but with a smaller stroke amplitude. The cycle-averaged v-velocity field is shown in Figure 11. When comparing the smaller stroke amplitude results with the previous case, shown in Figure 9 and Figure 10, it appears that the downwash does not distend as far as in the larger stroke amplitude case. While the magnitude of v-velocity in the down wash is higher, it is not a fair metric, as the general far-field wake does not form as strongly. Once again, the upward velocity occurs most prevalently at the stroke reversal locations. The smaller stroke range has a downwash that favors the initial motion direction greatly; the reason for this appears to rely heavily on the stability of the downwash region. For cases where the downwash is either unstable or not developed, the downwash favors the starting direction heavily.

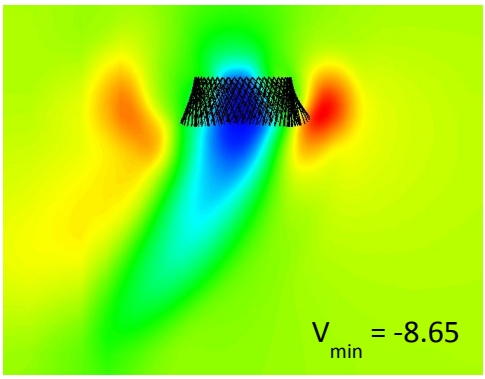

Figure 11: Cycle-averaged v-velocity contour for $A_x/c = 2$, $\omega_f/\omega_n = 1/6$

Instantaneous lift and drag coefficients are shown in Figure 12 for a sweep of various stroke amplitudes for a given frequency ratio. The drag coefficient peaks vary inversely with stroke amplitude; as the stroke range increases, the peaks (and averages) of drag decrease. An extreme range of motion ($A_x/c = 10$) is shown to illustrate the overall trend of the drag coefficient. As the stroke amplitude case increases maximally, the plate tends to incline to very low angles of attack, and the drag profiles within this long translation of the plate favor trends of static, fixed aircraft behaviors. However, as the stroke reverses, vortices are shed, and force oscillates while the plate changes direction. This is to be expected with flapping airfoils.

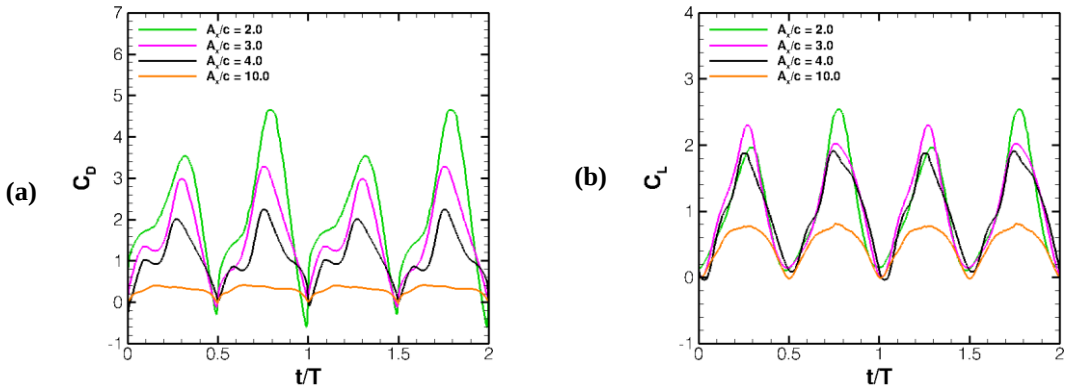

Figure 12: Stroke amplitude effects on instantaneous C_D and C_L for $\omega_f/\omega_n = 1/6$

Looking at the instantaneous lift profiles of the various stroke amplitudes, peak lift coefficients tend decrease as stroke amplitude increases. An interesting phenomena occurs for $A_x/c = 2$ and $A_x/c = 3$, for these two cases, the lift production peaks are not symmetric in the up and downstrokes. The smaller stroke amplitude favors peak lift in the upstroke, but as the amplitude increases, the downstroke favors peak lift, eventually producing symmetric lift peaks in both up and down strokes. Once again, the lift coefficient varies inversely with amplitude. However, the drag coefficient decreases more rapidly with stroke amplitude than in the lift coefficient, suggesting that the lift to drag ratio will benefit by increasing stroke amplitude.

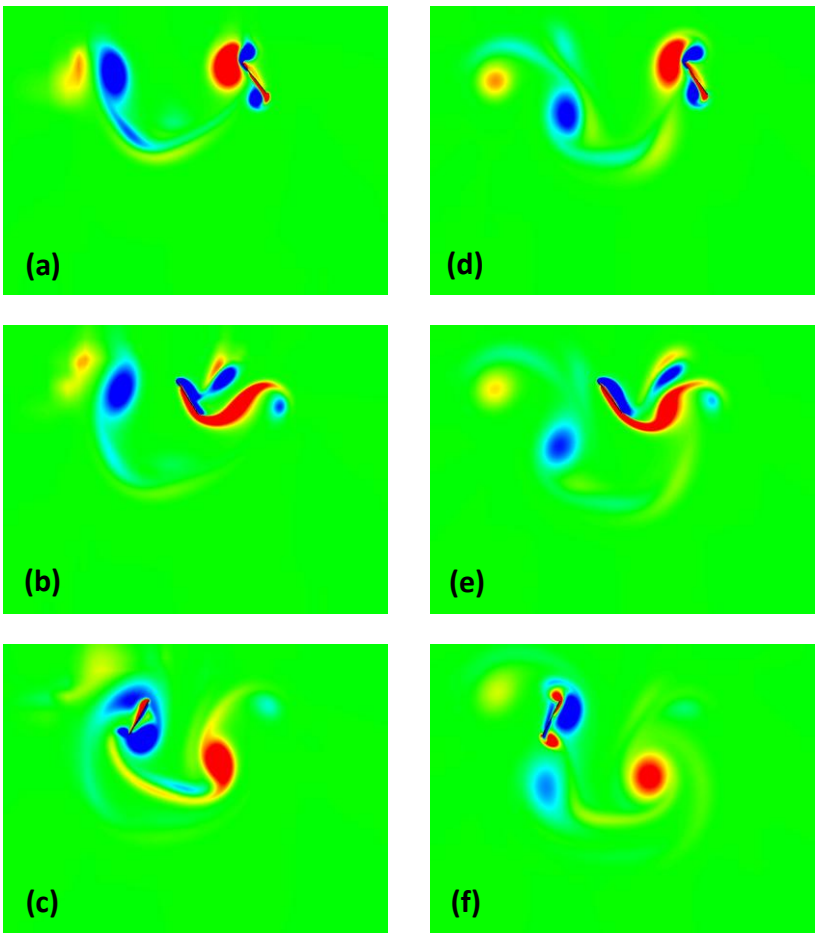

Figure 13: Stroke amplitude effects on vorticity contours for ω_f/ω_n = 1/6. (a-c) A_x/c = 3 and (d-f) A_x/c = 4. (a, d) t/T = 1.1, (b, e) t/T = 1.3, (c. f) t/T = 1.6.

To explain the variation at lift in instantaneous force, vorticity at several time locations within the same stroke are analyzed for the same frequency ratio, but with different stroke amplitudes, are shown in Figure 13. At t/T = 1.1, instantaneous lift coefficient is very similar for both stroke amplitude, which should be expected for a plate that is translating to the left, and the vorticity on the lee-side appears the same for both stroke amplitudes. However, at this instance, the drag differs, with the larger amplitude having lower drag. This is due to the clockwise rotating (blue) vortex colliding with the

windward side of the plate at the trailing edge. The collision of these two vortices results in a reduction in pressure acting on the windward side of the plate, reducing the drag. As the cycle progresses to t/T = 1.3, the longer stroke amplitude case has both lower drag and lower lift than the shorter stroke amplitude. The shorter stroke case has a larger, attached clockwise vortex on the lee-side, showing suggesting a higher lift. The shorter case also has a larger angle of attack, which, classically, suggests a higher drag value for translating plates. As the cycle progresses just beyond stroke reversal, into the upstroke, the trend continues. However, the vorticity remains quite different in comparison. This suggests that at stroke reversal, the better performing case could be gaining performance from the release of stored energy in the torsional spring.

Frequency Ratio Effects

The effect of frequency ratio on the general downwash, depicted as a cycle-averaged v-velocity contour plot, is shown in Figure 14.

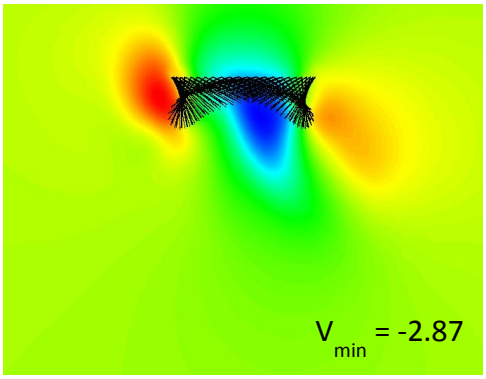

Figure 14: Cycle-averaged v-velocity contour for $A_x/c = 3$, $\omega_f/\omega_n = 1/3$

The frequency ratio is increased, making the hinge less rigid. As a result, the downwash is less prolonged, and has a smaller strength. The plate deflection is greater, reducing the angle of attack at midstroke. However, little benefits are gained at stroke reversal, where it has been noted that stiffer springs tend to aid in reversal, convecting the

shed vortices downstream more effectively. This was observed for all stroke amplitude ranges, decreasing stiffness diminished the downwash, which led to poor lift production.

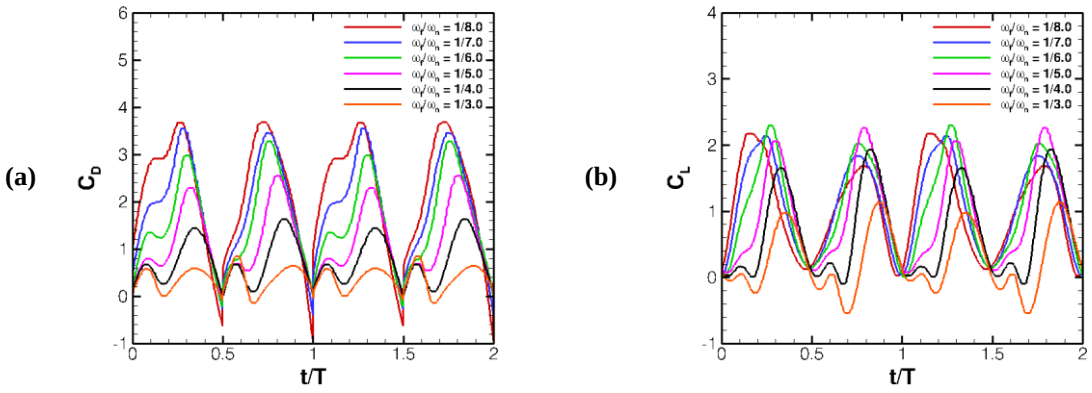

Figure 15: Frequency ratio effects on instantaneous C_D and C_L for $A_x/c = 3$

Figure 15 shows the effects of frequency ratio for a fixed kinematic profile on instantaneous lift and drag coefficients. It should be noted that more rigid (stronger torsional springs) hinges have smaller frequency ratios than the loose hinges. It is shown that trends remain consistent across all frequency ratios for drag coefficient. However, as stiffness reduces, the peak drag coefficients also reduced. This was expected, as the less rigid hinge deflects much easier, resulting in a lower angle of attack. Traditionally, lower angles of attack result in lower drag, and higher lift (in comparison to high angles of attack). This traditional thought does not hold for lift production in these cases. For loose hinges (high frequency ratios) two lift peaks occur for both the up and downstrokes. Typically, double peaks in lift production occur immediately after stroke reversal and are demonstrated in the events of wake capture. When timed correctly, wake capture can enhance lift. However, these loose hinge cases start out in negative lift oscillations, which diminish performance. From observations of vorticity animations, it was determined that these oscillations are a result of a collision with a previously shed wake that was not

properly convected downstream. As stiffness increases, so does the downwash production, causing less interaction between the plate and the shed vortices. This alleviates the affects of double oscillations in lift. It should also be noted that a bifurcation point may be present between ω_f/ω_n = 1/5 and 1/6, where at this point the asymmetric peak lift production changes which half stroke it favors. For more rigid hinges, the downstroke has a higher peak lift than in the upstroke. This is reversed for loose hinges. At this bifurcation point, it appears that lift is no longer increasing or decreasing with stiffness, but drag is still changing with stiffness. This suggests that a beneficial combination of stroke amplitude and frequency ratio could arise where an optimum lift to drag ratio may appear.

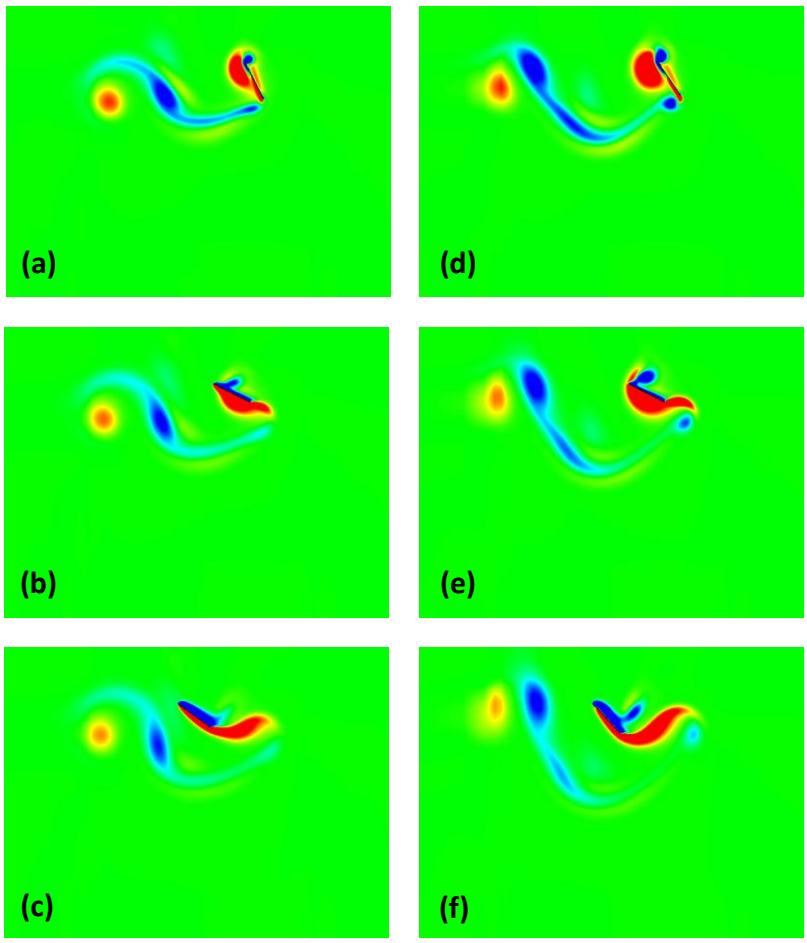

Figure 16: Frequency ratio effects on vorticity contours for $A_x/c = 3$, (a-c) $\omega_f/\omega_n = 1/4$ and (d-f) $\omega_f/\omega_n = 1/5$. (a, d) t/T = 1.1, (b, e) t/T = 1.2, (c. f) t/T = 1.3.

To better understand this phenomena where double peaking in lift occurs, ω_f/ω_n = 1/4 and 1/5 are selected for the same kinematics and vorticity snapshots are shown in Figure 16 for the same time steps where the discrepancies in force occur. Just after the start of the second downstroke, at t/T = 1.1, ω_f/ω_n = 1/5 has a higher lift, which is expected as a stronger LEV is forming for this case. This same case gains performance from recapturing the previously shed LEV, shown at t/T = 1.2. This trend continues as the stroke progresses to t/T = 1.3. It is shown that improvements in performance occur as

a result of beneficial wake capture, not utilized in loose hinges. At stroke reversal, if the torsional spring is stiff enough to where the energy released from the spring can act against the fluid momentum, the energy release will aid in shedding the previously formed LEV, and a new counter-rotating LEV will form, providing the opportunity for wake capture to occur. This is not observed for high frequency ratios (loose hinges).

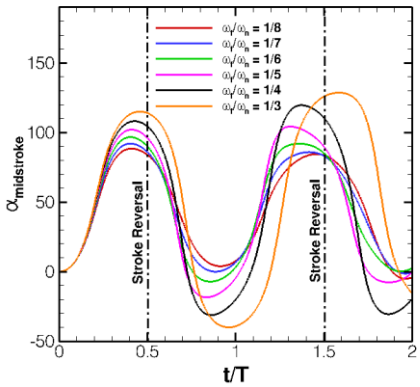

Figure 17: Frequency ratio effects on angle of attack for small A_x/c ($A_x/c = 2$)

An important region of kinematics should be discussed. For small stroke amplitudes (Ax/c < 2) the plate had very poor performance. Lift coefficients were negative for some cases. This is not an intuitive thought, as it is expected for hovering to generate positive lift values (even when small). But under further analysis, it is observed that the range of motion is too small for the torsional spring hinge to release any energy that is beneficial in rotating the plate and aiding the stroke reversal. In fact, as the downstroke progresses into the upstroke, traditionally well-performing hover kinematics should have a symmetric reversal of angle of attack from positive to negative or vice-versa. However, for hinged plates undergoing small stroke amplitudes, angle of attack reversal does not occur, meaning as the plate motion reverses, the angle of attack, in reference to the leading edge motion direction, is actual negative, which is responsible for

the negative lift production. This behavior is observed in Figure 17 across all frequency ratios for two chords range of motion. Obviously, cases where $A_x/c < 2$ should not be considered for design of a hovering MAV with a driven leading edge using a passive wing rotation mechanism.

Design Space Exploration

While the previous results subsections discussed the instantaneous effects of the design parameters, to find a suitable model for MAV design it is important to analyze the cycle-averaged force and power coefficients. Knowledge of these averaged values can be used as a metric that filters out oscillations within the stroke to predict a reliable value of lift and drag when estimating an ideal output from a design. The average values are plotted as a function of both stroke amplitude and frequency ratio to show the relationships for each metric with each design parameter. Stroke amplitudes less than two are not considered, as these were determined to be outside the realm of beneficial design possibilities.

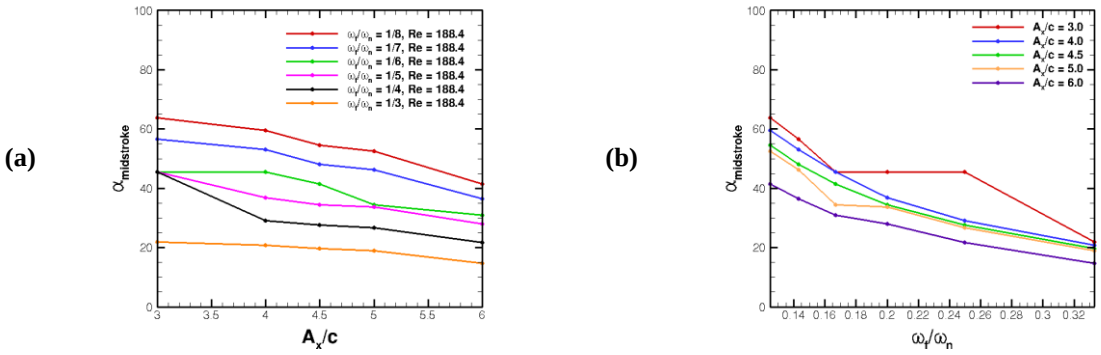

Figure 18: Cycle-averaged midstroke angle of attack for various stroke to chord and frequency ratios. (a) Variation of stroke amplitude and (b) frequency ratio.

The first useful quantity analyzed is the angle of attack at midstroke, averaged at the midpoint in up and downstrokes over four flapping cycles shown in Figure 18. Some

anomalies appear in the data, particularly at Ax/c = 3, ω_f/ω_n = ¼. It is unclear whether this is a true physical phenomenon or if the deflection at midstroke is misleading, as the peak may occur at a skewed moment in the stroke. Excluding this data point, angle of attack decreases as stroke amplitude increases across all frequency ratios. As frequency ratio increases, and the hinge spring becomes weaker, the angle of attack decreases for all $A_x/c > 2$. This particular anomaly is explained earlier, where the small range of motion coupled with a weak hinge does not reverse the angle of attack appropriately.

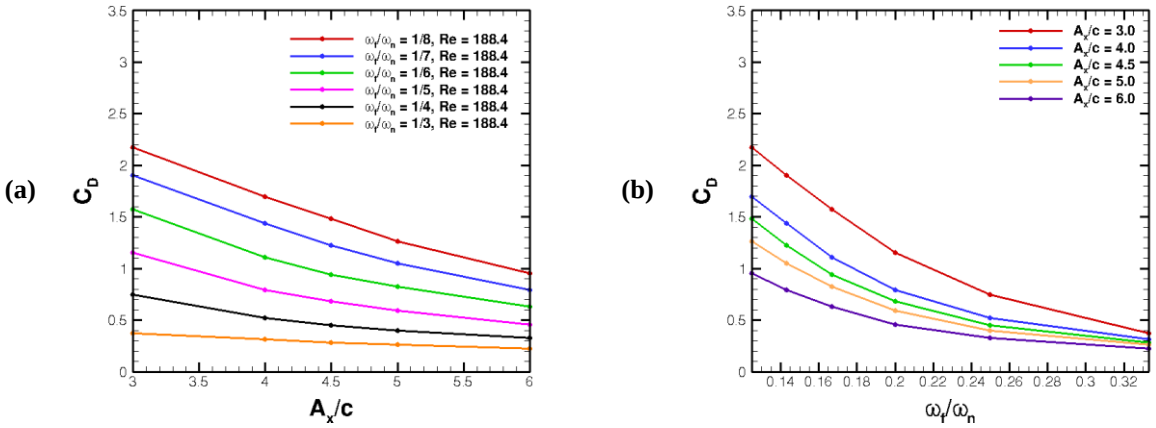

Figure 19: Cycle-averaged C_D comparison for various stroke to chord and frequency ratios. (a) Variation of stroke amplitude and (b) frequency ratio.

Drag coefficient decreases while stroke amplitude increases across all frequency ratios. Lower frequency ratio drag coefficients decrease more rapidly as amplitude increases in comparison to weak hinges. It is noted that as frequency ratio increases, stroke amplitude has a smaller effect on drag. Thus, performance is improved via a reduction in drag by choosing a weak hinge (high frequency ratio) or a stiff hinge that operates over a longer range of motion. This relationship is clearly shown in Figure 19.

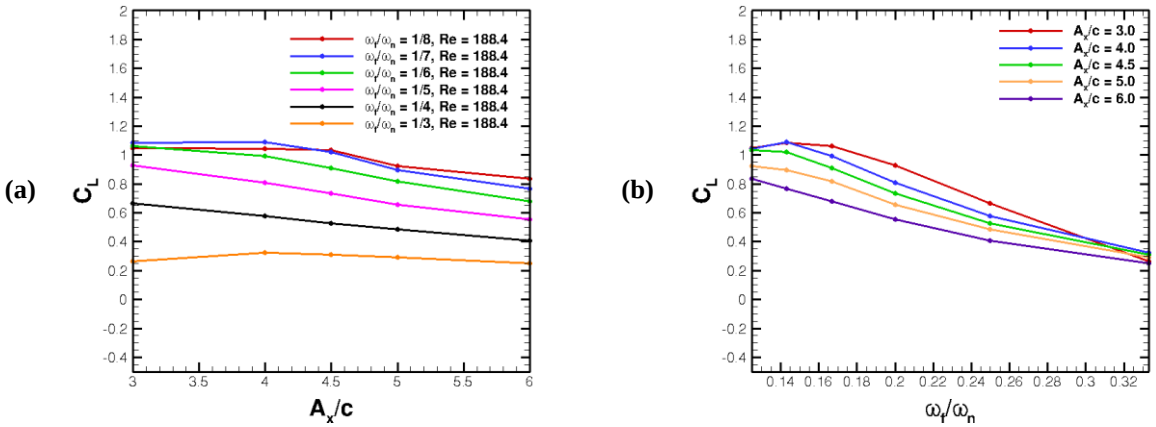

Figure 20: Cycle-averaged C_L comparison for various stroke to chord and frequency ratios. (a) Variation of stroke amplitude and (b) frequency ratio.

Lift is, arguably, the most often discussed metric for a hovering flapping wing MAV. The results of such are shown in Figure 20. For low frequency ratios stroke amplitude has little effect on cycle-averaged lift. However, for smaller amplitudes, the hinge stiffness variation causes a large deviation in lift. But, as stroke amplitude increases, weak hinges see a plateau and lift, and stiff hinges see a reduction in lift. In general, lower frequency ratios generate more lift for all stroke amplitudes, and, as range of motion increases, hinge stiffness has less of an effect on performance.

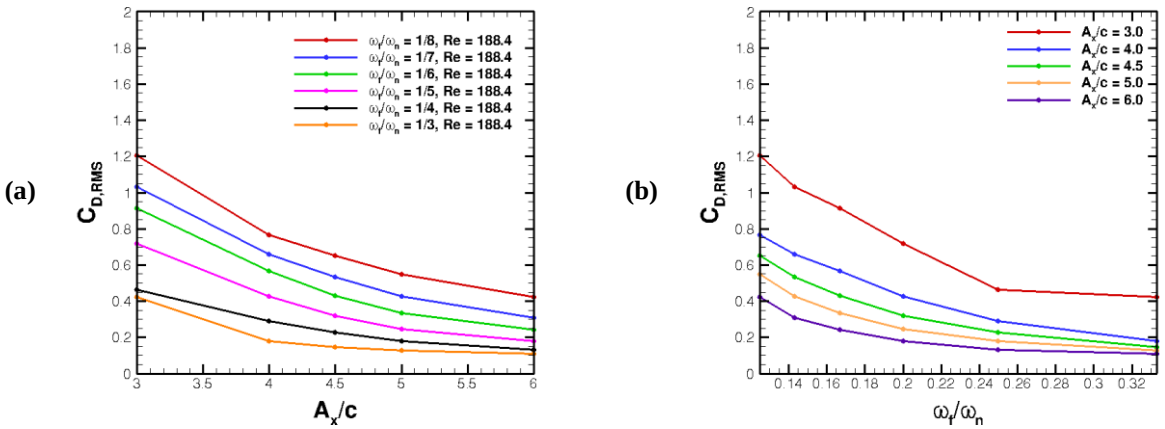

Figure 21: $C_{D,RMS}$ comparison for various stroke to chord and frequency ratios. (a) Variation of stroke amplitude and (b) frequency ratio.

Stability of force production is important to consider when designing a hovering MAV. If lift and drag both see high oscillations during the cycle, this has a tendency to cause instability in MAV flight. Sudden changes in force can induce aerodynamic moments, that when coupled with instability in the environment via gusts, can be detrimental to MAV performance. To this end, the root mean squared (RMS) values of drag and lift are analyzed in Figure 21 and Figure 22, respectively. Drag oscillations appear to be predominantly affected by stroke amplitude, with reduction occurring as the range of motion increases. Once again, for smaller stroke amplitudes, hinge stiffness carries an affect, with stiffness increasing the drag oscillations across the range of the study.

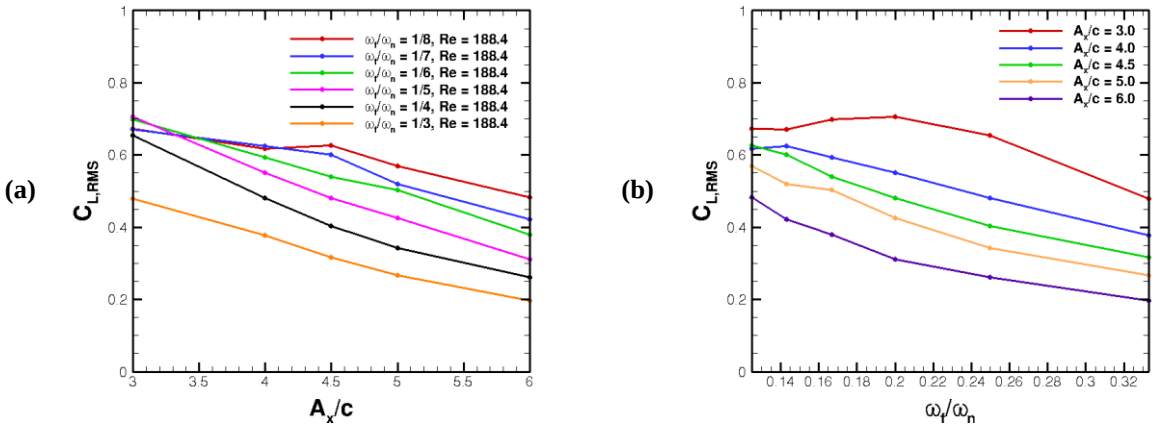

Figure 22: $C_{L,RMS}$ comparison for various stroke to chord and frequency ratios. (a) Variation of stroke amplitude and (b) frequency ratio.

Oscillations in lift are not readily decomposed into an effect of solely hinge stiffness or range of motion. Lift oscillations are reduced through an increase in either frequency ratio or stroke amplitude, with the latter having a greater effect on stability of lift production. Comparing both lift and drag together, stability is gained most adequately by selecting a large range of motion with a hinge of moderate stiffness.

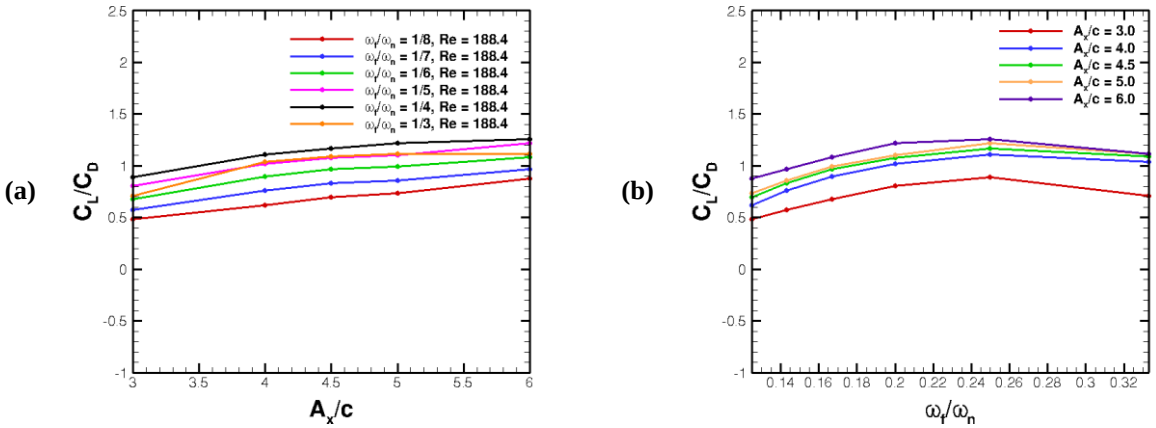

Figure 23: Cycle-averaged lift-to-drag ratio comparison for various stroke to chord and frequency ratios. (a) Variation of stroke amplitude and (b) frequency ratio.

The first quantity that can judge lift production outside a traditional sense of whichever has a higher lift coefficient champions the design is the lift-to-drag ratio.

While a specific amount of lift is required to sustain hover, this is important, as this quantity relates both lift and drag, where a high lift-to-drag ratio means that for a given amount of lift, drag is particularly lower, which in traditional aircraft methodologies means a better fuel economy. The same is true for flapping wings; lower drag on a reciprocating wing reduces the input force required to move the wing. This relates to input power, but is not directly proportional to power, as power relates the speed and rotation of the plate to the force required to move that plate. Lift-to-drag ratio is shown in Figure 23. Across all frequency ratios, the best lift-to-drag ratio occurs for $A_x/c = 6$. A bifurcation point occurs near $\omega_f/\omega_n = 1/4$. Below this point, more stiff hinges have worse performance, but beyond this point, a plateau occurs across the less stiff hinges with performance dictated solely by the range of motion.

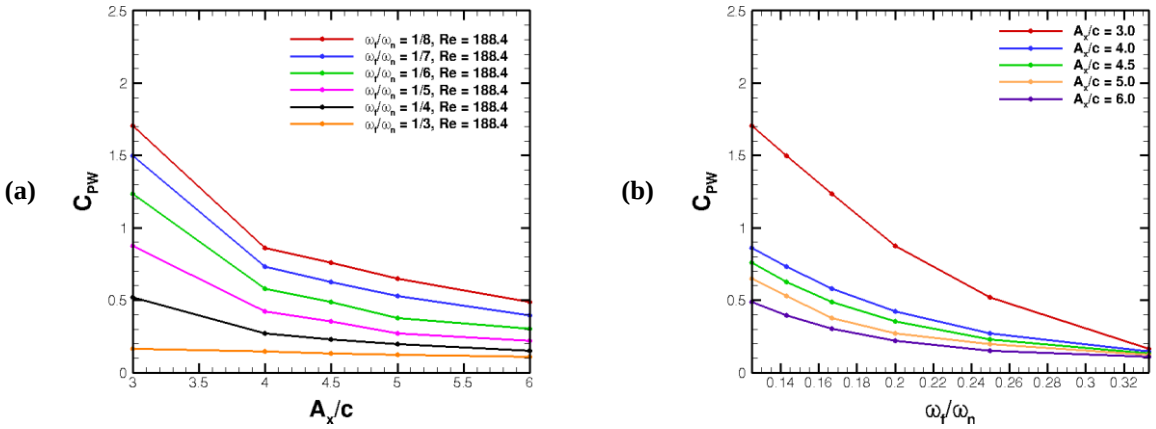

Figure 24: Cycle-averaged C_{PW} comparison for various stroke to chord and frequency ratios. (a) Variation of stroke amplitude and (b) frequency ratio.

While lift-to-drag ratio is a classically important performance metric, looking directly at the input power coefficient supplied at the point of prescribed kinematics is a better judge of performance. This evaluation is shown in Figure 24. As stroke amplitude increased, input power reduced, which increased performance. Similarly, power reduced

as frequency ratio increased. So the lowest input power occurs for the least rigid hinge over the largest range of motion.

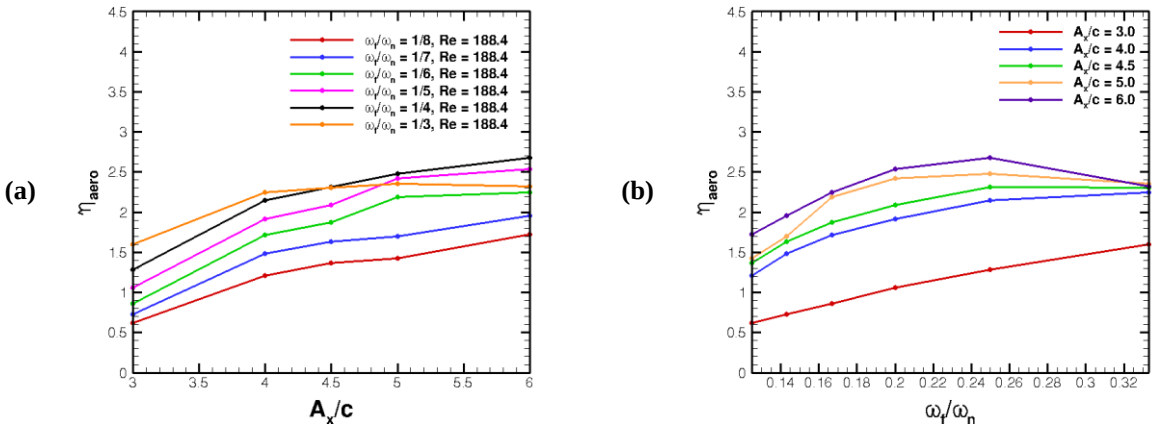

Figure 25: Cycle-averaged η_{aero} comparison for various stroke to chord and frequency ratios. (a) Variation of stroke amplitude and (b) frequency ratio.

The most important metric for design is the aerodynamic efficiency. This value relates the amount of required input power at the leading edge to the amount of lift generated. For design purposes, a concept that has a high amount of lift per unit input power is an ideal model. While the results appear convoluted, and overall trend of performance increase occurs as stroke amplitude increases. The best performing frequency ratio occurs for ω_f/ω_n = 1/4, which is the same bifurcation point observed for the trends of drag coefficient. Increasing the range of motion for this frequency ratio sees an improvement of performance. Frequency ratios beyond this point do not gain benefits by increasing amplitude. Likewise, small frequency ratios do not see as much benefit to by increasing the range of motion.

CONCLUSIONS

This work explored the effects of varying both hinge stiffness and kinematics to serves as guidelines for designing a leading edge actuated flapping wing MAV that experiences passive wing rotation and flow control. This particular concept MAV is one that is attractive as the performance can be tailored for mission specific duties, specifically in this case for hover. This work has a second purpose, and that is relating a basic MAV design to nature by way of understanding the parameters associated with insect flight and applying our understanding of their performance to a MAV.

An interesting thing occurs when a torsional spring is modeled in a flapping wing, the spring is able to store energy generated by the deflection of the plate due to the interaction with the fluid. When the stroke is reversed, this energy is released, causing the plate rotation to speed up. Traditionally, hinged plates without a leading edge torsional spring produce hovering kinematics that are akin to delayed rotation. However, the release of stored energy causes a change in the motion profile, which results in a performance boost. Tailoring this frequency ratio of the torsional spring, which, in turn, affects the hinge stiffness directly, can produce a stronger downwash and a better performing MAV design.

Hinge stiffness also controls the angle of attack during the stroke of the plate, tailoring this angle can equate to boosts in lift and reductions in drag, all of which affect the required input power to the wing. While kinematic profiles do affect the deflection of the plate as well as the stroke reversal, for a fixed motion profiles, choosing the right spring can create a boost in performance.

A region of kinematic profile is excluded from the design space due to complications with performance. This range includes all $A_x/c < 2$. The reason for such performance degradation is linked to the range of motion. For small amplitudes, the plate never has enough distance to travel to allow the plate to rotate through and give a positive angle of attack (in reference to the leading edge motion), especially for loose hinges. This is why loose (or free-to-pivot) hinges over small stroke amplitudes don't generate a positive or reasonable amount of lift. The stiff hinges over small amplitudes ($A_x/c < 2$) outperform the loose hinges because the spring allows the transfer of potential energy, in the spring, to kinetic energy, in the plate's rotation, at stroke reversal, allowing the plate to accrue a positive (and more beneficial) angle of attack before a loose (or free-to-pivot) hinge can do so under the same kinematics. This release of energy is essential in achieving benefits from wake capture as well as properly generating downwash.

It was observed that performance benefits were found for an increase in stroke amplitude via a reduction in drag, increase in lift, and decrease in RMS force oscillations. Because of this, lift-to-drag ratio, aerodynamic input power and efficiency all profited. For each stroke amplitude, stiffness can be tailored to improve flight performance. However, a bifurcation point at $\omega_f/\omega_n = ¼$ suggests that the ideal spring stiffness belongs at or near this frequency ratio.

To suggest a MAV concept design based on the results of this study, it would be beneficial to have the largest stroke amplitude possible within the design limitations. It is also suggested that the ideal frequency ratio governing hinge stiffness should be chosen as $\omega_f/\omega_n = ¼$. Another interesting thing can be noted about this choice of parameters. Reviewing the kinematics and known frequency ratios of dragonfly wings, this optimal

MAV design parameter choice coincides with the operating range of dragonflies. This suggests that one of nature's best flyers operates at a parameter range known to have an optimum flight performance discovered in this study, further supporting the idea that MAVs should be bio-inspired designs.

To summarize:

- *The torsional spring allows for a release of energy stored from deflection at the point of stroke reversal, improving performance and enhancing the wake capture mechanism.*
- *Stroke amplitudes of $A_x/c<2$ are not suited for hover*
- *Stroke amplitude increase*
    - *Decreases angle of attack, Increase lift, Reduces drag and power consumption*
    - *Decreases input power*
- *Increasing frequency ratio*
    - *Degrades downwash, diminishes cycle-averaged lift*
    - *Decreases input power*
- *Tailoring frequency ratio and stroke amplitude can find the best efficiency and lift production.*

FUTURE WORK

- *Developing a quasi-steady model for hinged plates*

While this work was comprehensive in the design space, it required a great deal of computational time (48+ hours per simulation). A wider variety of studies could be made, such as an in-loop control system, where the hinged body deflects in the presence of flow, and the resultant forces are applied to a control strategy. More complex mechanisms could be designed using similar works as this as well. To effectively reduce the simulation time while retaining accuracy of the force prediction, a similar model could be developed using these results to tailor this model. Creating a quasi-steady model for fluid body interaction would have a large number of uses, and with the success of quasi-steady models in flapping wing flight; this type of work could be accomplished in the short future.

- *Developing and validating flow-structure interaction solver*

In addition to reducing the simulation time to create a fast and accurate solution, a more in-depth model could be developed to allow the wing to deform with the flow rather than the body deflection. This is a more accurate depiction of an insect wing in nature. So for future work, developing a flow-structure interaction solver that has an accurate solver of both the fluid and body deformation could lead to a better understanding of insect flapping wing flight as providing a realistic tool for studying the physics behind deforming wings and complex MAV designs.

- *Study other maneuvers such as take-off and cruising*

While the focus of this work was to use the model to study the possibility of passive deflection for hovering flight, these methods could be adapted to further study other useful maneuver in flapping flight. This technology could be employed for studying and designing flapping wing flyers which are capable of take-off, cruising, and quick yaw turns.

- *Study the effects of gust*

In addition to this work, providing a control strategy for MAVs is a topic that is still new and relatively unstudied. A possible control strategy involved that active manipulation of the trailing edge of a wing while flapping to achieve complex maneuvers, or in some cases, such as take-off, to provide a sudden burst of force to lift from the ground. This strategy could also be used to provide flight stability in unpredictable environments where gust is probable or to maneuver around walls, where flight stability is difficult to manage, even in traditional aircrafts. Similar efforts and design of experiments from this work can be adapted to study this type of control strategy comprehensively.

APPENDIX A

Table 6: Parametric study results

A_x/c	ω_f/ω_n	C_D	C_L	C_L/C_D	$C_{D,RMS}$	$C_{L,RMS}$	C_{PW}	η_{aero}	$\Theta_{midstroke}$	$\alpha_{midtsroke}$
0.5	0.125	4.82	-0.11	-0.02	6.73	0.09	2.38	-0.05	1.0	89.0
0.5	0.143	4.89	-0.10	-0.02	6.78	0.08	2.43	-0.04	0.8	89.2
0.5	0.167	4.91	-0.08	-0.02	6.79	0.07	3.94	-0.02	0.7	89.3
0.5	0.200	4.92	-0.85	-0.17	6.79	0.07	2.47	-0.34	0.8	89.2
0.5	0.250	4.91	0.07	0.01	6.78	0.07	2.48	0.03	0.7	89.3
0.5	0.333	4.91	-0.08	-0.02	6.77	0.06	2.48	-0.03	0.7	89.3
1.0	0.125	2.73	0.72	0.26	1.19	0.52	1.57	0.46	23.1	66.9
1.0	0.143	1.90	-0.11	-0.06	1.94	0.34	1.29	-0.09	8.4	81.6
1.0	0.167	1.91	-0.49	-0.26	2.84	0.33	1.55	-0.31	11.7	78.3
1.0	0.200	2.48	-0.44	-0.18	3.32	0.31	1.17	-0.37	8.1	81.9
1.0	0.250	2.64	-0.52	-0.20	3.56	0.36	1.28	-0.41	7.1	82.9
1.0	0.333	2.83	-0.43	-0.15	3.72	0.30	1.36	-0.31	5.6	84.4
2.0	0.125	2.77	0.93	0.34	1.72	0.49	1.46	0.64	18.5	71.5
2.0	0.143	2.50	1.00	0.40	1.48	0.61	1.31	0.76	24.3	65.7
2.0	0.167	2.15	1.04	0.48	1.28	0.74	1.68	0.62	32.3	57.7
2.0	0.200	1.46	0.82	0.57	0.81	0.72	0.71	1.16	40.9	49.1
2.0	0.250	0.58	0.31	0.53	0.34	0.52	0.31	0.99	51.7	38.3
2.0	0.333	0.40	-0.23	-0.58	0.65	0.21	0.25	-0.93	36.7	53.3
3.0	0.125	2.17	1.05	0.48	1.20	0.67	1.70	0.61	26.3	63.7
3.0	0.143	1.90	1.09	0.57	1.03	0.67	1.50	0.72	33.5	56.5
3.0	0.167	1.58	1.06	0.67	0.91	0.70	1.23	0.86	44.6	45.4
3.0	0.200	1.15	0.93	0.81	0.72	0.71	0.88	1.06	44.6	45.4
3.0	0.250	0.75	0.66	0.89	0.46	0.65	0.52	1.28	44.6	45.4
3.0	0.333	0.37	0.26	0.71	0.42	0.48	0.16	1.60	68.1	21.9
4.0	0.125	1.69	1.04	0.61	0.77	0.62	0.86	1.21	30.6	59.4
4.0	0.143	1.44	1.09	0.76	0.66	0.63	0.73	1.48	36.9	53.1
4.0	0.167	1.11	0.99	0.90	0.57	0.59	0.58	1.72	44.5	45.5
4.0	0.200	0.79	0.81	1.02	0.43	0.55	0.42	1.91	53.2	36.8
4.0	0.250	0.52	0.58	1.11	0.29	0.48	0.27	2.15	60.9	29.1
4.0	0.333	0.31	0.33	1.04	0.18	0.38	0.14	2.25	69.2	20.8
4.5	0.125	1.49	1.03	0.70	0.65	0.63	0.76	1.36	35.5	54.5
4.5	0.143	1.23	1.02	0.83	0.53	0.60	0.62	1.63	41.9	48.1
4.5	0.167	0.94	0.91	0.96	0.43	0.54	0.48	1.88	48.6	41.4

4.5	0.200	0.68	0.73	1.08	0.32	0.48	0.35	2.09	55.6	34.4
4.5	0.250	0.45	0.53	1.16	0.23	0.40	0.23	2.31	62.5	27.6
4.5	0.333	0.28	0.31	1.09	0.15	0.32	0.13	2.31	70.4	19.6
5.0	0.125	1.26	0.92	0.73	0.55	0.57	0.65	1.42	37.5	52.5
5.0	0.143	1.05	0.90	0.86	0.43	0.52	0.53	1.70	43.7	46.3
5.0	0.167	0.82	0.82	0.99	0.33	0.50	0.37	2.19	55.6	34.4
5.0	0.200	0.59	0.66	1.10	0.25	0.43	0.27	2.42	56.2	33.8
5.0	0.250	0.40	0.49	1.22	0.18	0.34	0.20	2.47	63.3	26.7
5.0	0.333	0.26	0.29	1.11	0.13	0.27	0.12	2.36	71.2	18.8
6.0	0.125	0.95	0.83	0.87	0.42	0.48	0.48	1.72	48.5	41.5
6.0	0.143	0.79	0.77	0.97	0.31	0.42	0.39	1.95	53.6	36.4
6.0	0.167	0.63	0.68	1.08	0.24	0.38	0.30	2.25	59.1	30.9
6.0	0.200	0.45	0.55	1.22	0.18	0.31	0.22	2.54	62.1	27.9
6.0	0.250	0.32	0.41	1.26	0.13	0.26	0.15	2.68	68.3	21.7
6.0	0.333	0.22	0.25	1.11	0.11	0.20	0.11	2.32	75.3	14.7

Additional Methods

Working with PICAR3D, requires several user inputs such as the body mesh, fluid mesh, and prescribed velocity profile of the body. Because PICAR3D is still in developed, and maintained locally, there is currently no graphical user interface that allows for the treatment and formation of these files. To this end, several programs have been written that allows for: creation of solid and membrane bodies with triangular meshes, Cartesian grid fluid domains, and velocity profiles for all prescribed bodies at every time step. It is with this information, along with the computational parameters, such as numerical scheme choice, Reynolds number, time step information, and convergence criteria, that PICAR3D computes the velocity field in the fluid domain at every time step, the pressure within this field along with that acting on the body, and the updated position of the moving plate.

The plate body information, such as nodal arrangement and mesh coordinates, is performed using a custom code written in FORTRAN. The plate, an infinitely thin membrane, is comprised of one layer of nodes along its chord length, with three layers of nodes in the span wise direction (into the z-direction). PICAR3D requires a two-element thickness plate to be used for the simulation of 2-dimensional flows, as if treating the domain as a zero thickness slice of a 3-dimensional domain. The nodes are uniformly spaced along the chord wise direction, and for this work, 101 nodes are used (N = 101). The nodes form the basis of the plate, which is positioned into the initial position for the start of the simulation. The coordinates for the nodes are stored in a separate file to be interpreted in PICAR3D. The triangular elements are formed by assigning each element to three corresponding nodes, and recorded in the same file as the nodal coordinates. The convention of this arrangement as well the nodal assignments is shown in Figure 26 in the top-down view. Figure 26 denotes elements, e(n), in terms of element number, of which, the terminal nodes of that particular element are the three nodes surrounding the bounds of the triangular element. For a membrane plate, such as the one used, the total number of nodes is determined to be 3N, where N is the number of nodes per layer in the chord wise direction, and the total number of elements is determined to be 4*(N-1).

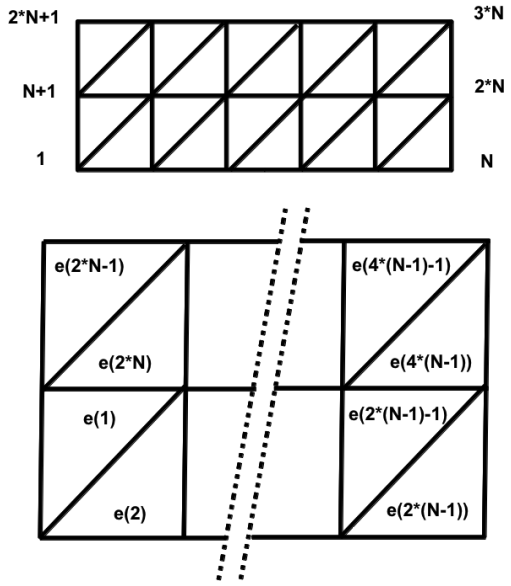

Figure 26: Unstructured surface triangular mesh diagram

Another program was developed to handle the plate motion, where the velocity components corresponding to every node are determined from a first order derivative of the position of the plate using a central difference scheme. While it is much simpler to denote the velocity of the nodes in terms of the first order derivative of the LE equations of motion, the program for determining velocity profiles was written to handle more complex motions determined from either input kinematics (determined from digitized data in journal papers) or from complex equations that handle both translation and rotation movements. While this work does not employ these features, other work has been performed using this tool. For this work using flow-body interaction for simulating a hinge, at every time step, the velocity components of the hinge node are recorded in a data file for interpretation by PICAR3D. At every time step, the hinge velocity in accordance with the coupling of the plate equations of motion and the fluid solver, is used to determine the motion of the resultant motion of the plate beyond the hinge. For

simulations not employing the flow-body interaction features, the plate motion can be fully prescribed, where all nodal velocity components are written to the data file for every time step and interpreted directly using PICAR3D.

REFERENCES

1. *Unsteady forces and flows in low Reynolds number hovering flight: two-dimensional computations vs robotic wing experiments.* **Wang, Z. Jane, Birch, James M. and Dickinson, Michael H.** 2004, Journal of Experimental Biology, pp. 449-460.

2. *On the roles of chord-wise flexibility in a flapping wing with hovering kinematics.* **Eldredge, J., Toomey, J. and Medina, A.** 2010, Journal of Fluid Mechanics, pp. 94-115.

3. *Influence of flexibility on the aerodynamic performance of a hovering wing.* **Vanella, M., et al.** 2009, Journal of Experimental Biology, Vol. 212, pp. 95-105.

4. *Computational fluid-body interaction of hinge connected flapping plate in hover.* **Wan, Hui, Dong, Haibo and Huang, George.** s.l. : AIAA, 2011. 49th AIAA Aerospace Sciences Meeting. Vols. 2011-0379.

5. *Passive wing pitch reversal in insect flight.* **Bergou, Attila J., Xu, Sheng and Wang, Z. Jane.** 2007, Journal of Fluid Mechanics, pp. 321-337.

6. *Flight performance of a dragonfly.* **Azuma, A. and Watanabe, T.** 1988, Journal of Experimental Biology, Vol. 137, pp. 221-252.

7. *The aerodynamics of free-flight maneuvers in drosophila.* **Fry, Steven N., Rosalyn, Sayaman and Dickinson, Michael H.** 2003, Science, Vol. 300, pp. 495-498.

8. *Mechanics of forward flight in bumblebees I. Kinematics and morphology.* **Dudley, R. and Ellington, C. P.** 1990, Journal of Experimental Biology, Vol. 148, pp. 19-52.

9. *The mechanics of flight in the hawkmoth Manduca Sexta. II. Aerodynamic consequences of kinematic and morphological variation.* **Wilmott, A. P. and**

Ellington, C. P. 1997a, Journal of Experimental Biology, Vol. 200, pp. 2723-2745.

10. *Measuring the angle of attack of beating insect wings: Robust three-dimensional reconstruction from two-dimensional images.* **Wilmott, A. P. and Ellington, C. P.** 1997b, Journal of Experimental Biology, Vol. 200, pp. 2693-2704.
11. *Flight and size constraints: Hovering performance of large hummingbirds under maximal loading.* **Chai, P. and Millard, D.** 1997, Journal of Experimental Biology, Vol. 200, pp. 2757-2763.
12. *The flight of birds: The significant dimensions, their departure from the requirements for dimensional similarity, and the effect on flight aerodynamics of that departure.* **Greenewalt, C. H.** 1975, Transactions of the American Philosophical Society, Vol. 65, pp. 1-67.
13. *On the natural freuquencies and mode chapes of dragonfly wings.* **Chen, J. S., Chen, J. Y. and Chou, Y. F.** 2008, Journal of Sound and Vibration, Vol. 313, pp. 643-654.
14. *The relationship between dragonfly wing structure and torsional deformation.* **Sunada, S. et al.** 1988, Journal of Theoretical Biology, Vol. 193, pp. 39-45.
15. *A second-order accuate pressure-correction schem for viscous incompressible flow.* **van Kan, J.** 3, 1986, SIAM Journal of Scientific Computing, Vol. 7, pp. 870-891.
16. *A versatile sharp interface immersed boundary method for incompressible flows with complex boundaries.* **Mittal, R., Dong, H., Bozkurttas, M., Najjar, F. M., Vargas, A., and von Loebbecke, A.** 2008, Journal of Computational Physics, Vol. 227, pp. 4825-4852.

17. *Wake topology and hydrodynamic performance of low-aspect-ratio flapping foils.* **Dong, H., Mittal, R. and Najjar, F. M.** 2006, Journal of Fluid Mechanics, Vol. 566, pp. 309-343.

18. *An integrated analysis of a dragonfly in free flight.* **Dong, Haibo, et al.** s.l. : AIAA, 2010. 40th AIAA Fluid Dynamics Conference and Exhibit. Vols. 2010-4339.

19. *Vortex shedding and frequency selection in flapping flight.* **Wang, Z. Jane.** 2000, Journal of Fluid Mechanics, Vol. 410, pp. 323-341.

20. *Energy-minimizing kinematics in hovering insect flight.* **Berman, G. J. and Wang , Z. J.** 2007, Journal of Fluid Mechanics, Vol. 582, pp. 153-168.

21. *A two-dimensional computational study on the fluid-structure interaction cause of wing pitch changes in dipteran flapping flight.* **Ishihara, D., Horie, T. and Denda, M.** 2009, Journal of Experimental Biology, Vol. 212, pp. 95-105.

22. *Vortex formation of freely falling plates.* **Wan, Hui, Dong, Hui and Liang, Zongxian.** s.l. : AIAA, 2012. 50th AIAA Aerospace Sciences Meeting. Vols. 2012-1079.

23. *Unsteady flow and its reduced order modeling of finite-aspect-ratio foils.* **Liang, Zongxian, et al.** s.l. : AIAA, 2012. 50th AIAA Aerospace Sciences Meeting. Vols. 2012-1207.

24. *Viscous flow normal to a flat plate at modeerate Reynolds numbers.* **Dennis, S. C. R., et al.** 1993, Journal of Fluid Mechanics, Vol. 248, pp. 605-635.

25. *Simulations of the viscous flow normal to an impulsively started and uniformly accelerated flat plate.* **Koumoutsakos, P. and Shiels, D.** 1996, Journal of Fluid Mechanics, Vol. 328, pp. 177-227.

26. *Analysis of a hinge-connected flapping plate with an implemented torsional spring model.* **Gaston, Zachary, et al.** s.l. : AIAA, 2012. 50th AIAA Aerospace Sciences Meeting. Vols. 2012-0298.

27. *Aerodynamic characteristics of dragonfly wing sections compared with technical aerofoils.* **Kesel, Antonia.** 2000, Journal of Experimental Biology, Vol. 203, pp. 3125-3135.

28. *A computational study of the aerodynamic performance of a dragonfly wing section in gliding flight.* **Vargas, Abel, Mittal, Rajat and Dong, Haibo.** 2008, Bioinspiraiton and Biomimetics, Vol. 3, pp. 1-13.

29. **Shyy, w. et al.** *Aerodynamics of Low Reynolds Number Flyers.* s.l. : Cambridge University Press, 2008. pp. 101-158.